






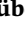
RESEARCH ARTICLE

10.1029/2021SW002824

Special Section:

Space Weather Impacts on Electrically Grounded Systems at Earth's Surface

Climatological Statistics of Extreme Geomagnetic Fluctuations With Periods From 1 s to 60 min

N. C. Rogers¹ , J. A. Wild¹ , E. F. Eastoe¹ , and J. Hübert² 

¹Lancaster University, Lancaster, UK, ²British Geological Survey, Edinburgh, UK

Key Points:

- Occurrence rates of extreme geomagnetic fluctuations (dB_n/dt) are mapped against magnetic local time, latitude, and season
- The log frequency (or timescale) dependence of dB_n/dt is well modeled by quadratic functions parameterized by geomagnetic latitude
- Electric fields calculated at three UK sites peak at periods of 20 min at the 99.97th percentile but 0.5–2 min for 1/100-year events

Correspondence to:

N. C. Rogers,
n.rogers1@lancaster.ac.uk

Citation:

Rogers, N. C., Wild, J. A., Eastoe, E. F., & Hübert, J. (2021). Climatological statistics of extreme geomagnetic fluctuations with periods from 1 s to 60 min. *Space Weather*, 19, e2021SW002824. <https://doi.org/10.1029/2021SW002824>

Received 14 JUN 2021
Accepted 9 OCT 2021

Abstract Using a global database of 125 magnetometers covering several decades, we present occurrence statistics for fluctuations of the horizontal geomagnetic field (dB_n/dt) exceeding the 99.97th percentile ($P_{99.97}$) for both ramp changes (R_n) and the root-mean-square (S_n) of fluctuations over periods, τ , from 1 to 60 min and describe their variation with geomagnetic latitude and magnetic local time (MLT). Rates of exceedance are explained by reference to the magneto-ionospheric processes dominant in different latitude and MLT sectors, including ULF waves, interplanetary shocks, auroral substorm currents, and traveling convection vortices. By fitting generalized Pareto tail distributions above $P_{99.97}$, we predict return levels (RLs) for R_n and S_n over return periods of between 5 and 500 years. $P_{99.97}$ and RLs increase monotonically with frequency ($1/\tau$) (with a few exceptions at auroral latitudes) and this is well modeled by quadratic functions whose coefficients vary smoothly with latitude. For UK magnetometers providing 1-s cadence measurements, the analysis is extended to cover periods from 1 to 60 s and empirical Magnetotelluric Transfer functions are used to predict percentiles and return levels of the geoelectric field over a wide frequency range (2×10^{-4} to 4×10^{-2} Hz) assuming a sinusoidal field fluctuation. These results help identify the principal causes of field fluctuations leading to extreme geomagnetically induced currents (GIC) in ground infrastructure over a range of timescales and they inform the choice of frequency dependence to use with dB_n/dt as a GIC proxy.

Plain Language Summary On rare occasions, an eruption on the sun's surface sends a cloud of energetic electrically charged particles out into interplanetary space. When this arrives at the Earth, it can cause large electrical currents to flow around the magnetic field surrounding the Earth (the "magnetosphere") and through the upper atmosphere. These currents are detected on the ground as fluctuations in the magnetic field and may induce unwanted electrical currents in high-voltage power lines or other long metallic cables and pipelines. The rate of change of the magnetic field is used together with measurements of ground conductivity to calculate the electric field that drives such "geomagnetically induced currents." In this study, we report the rate of occurrence of extremely rapid fluctuations in the magnetic field and how this depends on latitude and time of day. We model the dependence of the size of the fluctuations on their timescales since this is important for estimating the subsequent response of the power grid. The patterns of extreme occurrences are explained by reference to known electrical current systems and waves in the magnetosphere and upper atmosphere, and we use statistical methods to predict the size of fluctuations expected over periods from 5 to 500 years.

1. Introduction

Large electrical currents are occasionally induced in ground-based infrastructure as a result of rare and intense currents in the ionosphere or magnetosphere. These geomagnetically induced currents (GICs) have been identified as a substantial hazard to national infrastructure (Cannon et al., 2013; Hapgood et al., 2021) since they may cause catastrophic failure in high-voltage (HV) electricity supply networks (Gaunt, 2016; Oyedokun & Cilliers, 2018; Thomson et al., 2010), damage long-cable communication systems (Nevanlinna et al., 2001), and cause railway signaling errors (Boteler, 2021; Eroshenko et al., 2010; Wik et al., 2009). The cumulative effect of GICs above a certain threshold may also cause corrosion in oil and gas pipelines (Boteler, 2000; Pulkkinen et al., 2001). The science of GICs and their effects is reviewed in Knipp (2011, Chapter 13) and Buzulukova (2017, Chapter 8).

Modeling the risk of extreme GICs requires a statistical characterization of the geoelectric field, E , induced by electrical currents in the ionosphere and magnetosphere. This information may, for example, be

© 2021. The Authors.

This is an open access article under the terms of the [Creative Commons Attribution License](https://creativecommons.org/licenses/by/4.0/), which permits use, distribution and reproduction in any medium, provided the original work is properly cited.

combined with a model of electrical impedances in a HV electricity network (Boteler & Pirjola, 2017) to determine the “return level” (RL) of GIC expected in a “return period (RP)” of 100 years or more. Direct measurements of E are often subject to contamination from anthropogenic electromagnetic interference and require an experienced expert to remove noise and biases (Kelbert et al., 2017). They are also not global in extent, and do not cover the decades required for accurate prediction over long RPs. For climatological studies, it is therefore expedient to instead use an archive of measurements of the rate of change of the horizontal component of the geomagnetic field, dB_h/dt , measured at ground level. Using Faraday’s law of induction (Faraday, 1832) and magneto-telluric (MT) theory (Cagniard, 1953; Chave & Jones, 2012), these may be combined with a model of the local ground conductivity to determine climatological statistics for E . Alternatively, E may be derived using collocated measurements of ground impedance at a magnetometer site.

The calculation of E requires knowledge of both the temporal spectrum of geomagnetic oscillations and the frequency dependence of the surface impedance. Databases of impedance tensors are increasingly available for public use (e.g., Kelbert et al., 2011, 2018) and can cover a wide frequency range corresponding to periods from milliseconds to hours. The most effective source of geoelectric fields producing damaging GIC in power transmission lines lie in 1–1,000 s period oscillations (Barnes et al., 1991; Kappenman, 2004) and electricity companies have identified that fluctuations on timescales from tens of seconds to over an hour have led to vulnerability of HV electricity networks to GIC (e.g., Girgis & Vedante, 2012; NERC, 2017). A well-reported example is the geomagnetic storm of March 13, 1989 in which the 21 GW Hydro-Québec power supply failed for 9 hr following horizontal geomagnetic field fluctuations $|dB_h/dt|$ of ~ 500 nT/min (p. 640, Knipp, 2011).

The frequency of the induced E field fluctuations and consequent GICs is much less than the frequency of HV electricity networks (50 or 60 Hz) and so is often modeled as a quasi-direct current. Currents of more than a few amperes sustained over periods similar to the thermal time constants of the components of a HV transformer—typically 30–45 min—may cause irreversible damage resulting in power failures (Erinmez et al., 2002; Girgis & Vedante, 2012; IEEE, 2015, p. 8; Molinski, 2002; NERC, 2017). GICs generated by field fluctuations with periods longer than 1 hr have amplitudes too small to be of concern, while sub-1-s fluctuations are heavily damped by inductances in electric power systems (Boteler & Pirjola, 2017). Understanding the climatology of extreme $|dB_h/dt|$ over periods from 1 s to 1 hr should, therefore, help to quantify the GIC risk to electrical power systems.

Large-scale statistical surveys often exploit measurements at 1-min resolution, in large part enabled by the successful SuperMAG project (Gjerloev, 2011), thus many have examined only the 1-min changes in B_h (denoted R_1), with this metric being adopted as a proxy for GICs (e.g., Thomson et al., 2011; Viljanen et al., 2015, 2001). However, probability distributions of $|dB_h/dt|$ are observed to depend strongly on the time resolution (or sample averaging period) of the B field measurements, with lower amplitudes at longer sampling intervals due to the effect of smoothing. In recent years, an increasing number of magnetometer operators have offered users measurements at 1-s cadence and so the question arises as to which temporal resolution to apply when using $|dB_h/dt|$ as a proxy indicator for GIC. Modeling by Pulkkinen et al. (2006) showed that smoothing the B -field components from their native resolution of 1 s up to 60 s reduced the amplitude of $|dB_h/dt|$ by 80% while the computed peak E -field amplitudes were reduced by only 20%, the inference being that a 60-s (but no more) sample interval is acceptable as a proxy to use for E -field (and hence GIC) calculations. Other studies have noted that rather than taking R_1 as a proxy for GIC, a better performing indicator was obtained by taking an average dB_h/dt over 20-min (Tóth et al., 2014) or 30 min (Viljanen et al., 2015), while others have used the hourly range or standard deviation (Beamish et al., 2002; Danskin & Lotz, 2015; Nikitina et al., 2016) or 3-hourly range indices as a proxy (Trichtchenko & Boteler, 2004).

In several cases, the magnitude of B_h relative to its quiet-day value (often denoted ΔH) has provided a better proxy for GIC than dB_h/dt (Pulkkinen et al., 2010; Tóth et al., 2014; Watari et al., 2009). Pirjola (2010) showed how this is more likely to arise in regions for which there is an upper, highly conductive layer overlying a deeper layer of low conductivity. Heyns et al. (2020) presented examples of GIC amplitudes and phases matching closely to the 20-min period fluctuations of the field (ΔH), which were poorly represented by high-cadence dB_h/dt indicators, while dB_h/dt was a better indicator of the rapid field variation that occurred during Sudden Commencements, which often initiate geomagnetic storms. Heyns et al. (2020) explained

that this is because the B field (or ΔH) has low-frequency components that are deweighted when taking the time derivative—for example, if $B_h = B_0 \exp(i\omega t)$, then frequency components of $|dB_h/dt|$ are weighted by the factor $1/\omega$. Consequently, 1-s resolution dB_h/dt measurements ($R_{1/60}$) would be even less effective as a proxy for GIC (compared to R_1) caused by field fluctuations of a much longer period. Power networks can respond strongly to B -field fluctuations over tens of minutes, indicative of finite reactive impedances in the network components and assumptions that the geomagnetic driving is d.c. in nature may be insufficient to replicate the observed GIC (Heyns et al., 2020; Jankee et al., 2020).

The study of extreme geomagnetic fluctuations over a range of periods yields much information about the causes and impacts of GIC as well as the drivers of these fluctuations. The ionospheric and magnetospheric processes contributing to dB_h/dt over a 1-min period will differ greatly from those at 60 min and will depend on the latitude, magnetic local time (MLT), season, and other factors. The principal drivers of short transients (timescales of minutes) may be categorized into the following phenomena:

1. **Sudden Commencements (SC):** Interplanetary shocks arriving in the solar wind, which generate a sudden eastward (dusk-to-dawn) Chapman-Ferraro current at the dayside magnetopause, are observed as Sudden Commencements (SC) in magnetograms (Fiori et al., 2014; Kappenman, 2003; Smith et al., 2019). The characteristic rapid magnetic field variation may be short-lived, lasting several minutes or up to an hour (Knipp, 2011, p. 496) and are associated with dB_h/dt of up to 30 nT/min at low geomagnetic latitudes ($<40^\circ$) or up to a maximum of 270 nT/min in the auroral zone ($\sim 65^\circ$ geomagnetic latitude) (Fiori et al., 2014).
2. **Auroral substorm onsets:** A substorm is the sudden brightening and expansion of auroral arcs resulting from bursts of energetic electron precipitation from the magnetotail (Akasofu, 2017; Ieda et al., 2018). This enhances the ionization and electrical conductivity of the ionospheric E region allowing strong Hall currents to flow, most often in a westward direction, which manifest in magnetograms as a rapid decline in the north component of the geomagnetic field, B_N . Substorm onsets have been categorized by Newell and Gjerloev (2011) from the SML geomagnetic index (which measures the lower envelope of B_N) as a reduction of at least 45 nT over 3 min followed by a mean level at least 100 nT below the initial value during the half-hour following onset.
3. **Day-time Magnetic Impulse Events (MIE):** Pairs of up- and down-field aligned currents generated by a pulse in dynamic pressure at the dayside magnetopause couple into the ionosphere as Traveling Convection Vortices (TCV) at latitudes in the vicinity of the dayside cusp/cleft ($\sim 77\text{--}78^\circ$ magnetic) (Engebretson et al., 2013; Friis-Christensen et al., 1988; Kataoka et al., 2003; Lanzerotti et al., 1991; Zesta et al., 2002). Magnetometers in this region observe the ionospheric Hall current loops (a pair of vortices) as isolated magnetic impulse events (MIE) in magnetograms, lasting typically 5–15 min with amplitudes of typically 50–200 nT or up to a maximum of 400 nT (Kataoka et al., 2003; Lanzerotti et al., 1991). Several mechanisms have been postulated to explain the generation of TCVs near the dayside magnetopause, including bursts of magnetic field line reconnection (flux transfer events), solar wind pressure pulses, plasma injections into the low-latitude boundary layer, Kelvin-Helmholtz instabilities, and perturbations of the ion foreshock upstream of the Earth's bow shock (see references in Engebretson et al., 2013; Kataoka et al., 2003). In general, TCVs are defined so as to exclude sudden commencement perturbations associated with a large interplanetary shock (e.g., Pilipenko et al., 2019).
4. **Night-time Magnetic Perturbation Events (MPE):** MPEs are a broad class of large (hundreds of nT), localized, 5–10 min unipolar or bipolar pulses of B_h , which occur in the auroral zone during substorms, but are not necessarily associated with substorm onsets (Apatenkov et al., 2020; Belakhovsky et al., 2019; Dimmock et al., 2019; Engebretson et al., 2020, 2021; Engebretson, Pilipenko, et al., 2019; Engebretson, Steinmetz, et al., 2019; Viljanen, 1997). They arise from transient phenomena in the magnetotail such as bursty bulk flows (BBFs) (Angelopoulos et al., 1992; Wei et al., 2021), dipolarising flux bundles (Liu et al., 2014), poleward-expanding discrete aurorae passing over the magnetometer site (Ngwira et al., 2018), and small-scale rapidly moving ionospheric current vortices (Apatenkov et al., 2020).

A significant number of GIC events occur under geomagnetic storm conditions at auroral and mid-latitudes due to sustained ULF pulsations in the Pc5 band (2.5–10-min period field oscillations (Baker et al., 2003; McPherron, 2005; Pilipenko et al., 2010; Ziesolleck & McDiarmid, 1995)). These may be driven by Alfvén wave Kelvin-Helmholtz instabilities in the magnetosphere and are often initiated by the arrival of a shock

in the solar wind or a high-speed solar wind stream (>500 km/s) (Engebretson et al., 1998; Hao et al., 2019; Pahud et al., 2009; Vennerstrøm, 1999; Zhang et al., 2010). In addition, auroral omega bands (Apatenkov et al., 2020; Belakhovsky et al., 2019) may manifest in magnetograms as quasi-periodic (4–40 min) “Pi3” or “Ps6” geomagnetic fluctuations on the morning side during the recovery phases of substorms (Jorgensen et al., 1999; Saito, 1978; Wild et al., 2000) or during substorm expansions in the midnight sector (Wild et al., 2011).

B -field fluctuations over tens of minutes may also arise from the expansion and recovery phases of substorms in the auroral zone (Freeman et al., 2019; Pothier et al., 2015): The substorm expansion phase typically lasts 25–40 min (Pothier et al., 2015) followed by a more gradual recovery phase. Changes over an hour or more may arise from slow changes and movements of an electrojet over a magnetometer station or from gradual changes of the magnetospheric inner ring current intensity during the main and recovery phases of a geomagnetic storm.

At very high latitudes (poleward of the dayside cusp) and under conditions of northward interplanetary magnetic field (IMF) and large dipole tilt (e.g., at summer noon), magnetic fluctuations may be associated with the merging of “overdraped” tail-lobe field lines with the IMF (Crooker, 1992; Watanabe et al., 2005). Rogers et al. (2020) postulated that field-line reconnections may drive impulsive “Region-0” field-aligned currents (Milan et al., 2017; Wang et al., 2008) into this region that could manifest as large $|dB_h/dt|$ fluctuations at the surface.

In this study, we have extended a global climatological statistical model of extreme 1-min fluctuations, R_1 (Rogers et al., 2020), to include the magnitude and frequency of occurrence of extreme $|dB_h/dt|$ over sampling periods between 1 and 60 min, both as ramp changes (applying a moving average of the geomagnetic field measurements) and as a root-mean-square (RMS) of the R_1 values over n -minute periods that we denote S_n for $n = 1–60$ (defined explicitly in Section 2). The latter is a measure of the sustained power in extreme geomagnetic field fluctuations, which is important in modeling the risk to transformer components due to heating, for example. Our study complements that of Love, Coïsson, and Pulkkinen (2016) who provided an analysis of extreme $|dB_h/dt|$ over 1- and 10-min periods (R_1 and R_{10}), and the RMS of R_1 over 10 min (S_{10}). Wintoft (2005) and Wintoft et al. (2005) also chose to study S_{10} as a predictor of the RMS GIC amplitude. Part of our study will focus on three UK magnetometer sites and as such complements the work of Beamish et al. (2002)—who examined the hourly standard deviation of 1-min B -field north and east components (independently), a measure similar to the S_{60} calculated in this paper—and the works of Beggan et al. (2013) and Beggan (2015), who estimated extreme E -field and GICs for the UK national grid at 100- and 200-year RPs using UK ground conductivity models for 2- and 10-min period fluctuations of the inducing B -field, with amplitudes inferred from predicted extremes of R_1 presented by Thomson et al. (2011).

In Section 2, we describe the processing of magnetometer measurements data set and the determination of extreme values for $|dB_h/dt|$ as both ramp changes and RMS fluctuations. Section 3 presents the latitude and MLT distributions of large percentiles and projected extreme values for a range of sampling frequencies and develops a global model to characterize the dependences on sampling frequency. The frequency range is extended up to 1 Hz sampling for three UK sites and for these locations empirical MT transfer functions (or surface impedance matrices) are used to predict high percentiles and extreme values of the geoelectric field.

2. Measurements

Magnetic field measurements (magnetograms) were obtained from 125 magnetometers in the global SuperMAG collaboration (Gjerloev, 2011) at sites for which at least 20 years of data were available, with an average of 28 years' data per site. Table 1 provides the locations of these magnetometer sites in geodetic and corrected geomagnetic (CG) coordinates (Laundal & Richmond, 2017; Shepherd, 2014). Due to the secular variation of the Earth's main field, CG coordinates are given as averages over all the years in which magnetometer data were available at each site. In this study, we consider only the north and east components of the magnetic field (B_N and B_E , respectively) in local magnetic coordinates (Gjerloev, 2012) neglecting the downward vertical field component, B_z , which contributes little to GICs in surface-based infrastructure. The magnetograms provided by SuperMAG had already been cleaned and manually inspected to remove most artificial sudden changes in the baseline (offsets), spikes, and gradual slopes (Gjerloev, 2012). Nonetheless,

Table 1
Locations of the 125 Magnetometer Sites

IAGA code	Location	Geodetic latitude (°N)	Geodetic longitude (°E)	Mean corrected geomagnetic latitude (°N)	Mean corrected geomagnetic longitude (°E)
ABG	Alibag, India	18.62	72.87	12.19	145.59
ABK	Abisko, Sweden	68.35	18.82	65.29	101.98
AMS	Martin-de-Viviès, Amsterdam I.	-37.8	77.57	-49.10	138.76
AND	Andenes, Norway	69.3	16.03	66.53	99.89
API	Apia, Samoa	-13.8	188.22	-15.59	-97.20
ASC	Ascension Island	-7.95	345.62	-10.37	56.47
ASP	Alice Springs, Australia	-23.77	133.88	-34.06	-152.63
ATU	Attu, India	67.93	306.43	74.19	38.37
BDV	Budkov, Czechia	49.07	14.02	44.40	89.37
BEL	Belsk, Poland	51.83	20.8	47.55	96.06
BFE	Brorfelde, Denmark	55.62	11.67	52.03	89.51
BJN	Bjørnøya, Svalbard	74.5	19.2	71.47	107.94
BLC	Baker Lake, Canada	64.33	263.97	74.01	-32.85
BMT	Beijing Ming Tombs, China	40.3	116.2	34.81	-170.72
BOU	Boulder, USA	40.13	254.77	49.04	-40.52
BRW	Utqiagvik, Alaska, USA	71.3	203.25	69.95	-109.37
BSL	Bay St Louis, USA	30.35	270.37	41.23	-19.39
CBB	Cambridge Bay, Canada	69.1	255	77.32	-51.99
CBI	Chichi-jima, Japan	27.15	142.3	19.83	-146.53
CDC	Cape Dorset, Canada	64.2	283.4	73.54	2.26
CHD	Chokurdakh, Russia	70.62	147.89	65.11	-146.75
CLF	Chambon-la-forêt, France	48.02	2.27	43.42	79.46
CMO	College, Alaska, USA	64.87	212.14	64.99	-96.46
CNB	Canberra, Australia	-34.1	150.7	-43.93	-131.74
CSY	Casey, Antarctica	-66.28	110.53	-80.79	156.40
CTA	Charters Towers, Australia	-20.1	146.3	-29.15	-139.40
CZT	Port-Alfred, Crozet Is.	-46.43	51.87	-53.25	106.05
DAW	Dawson City, Canada	64.05	220.89	65.94	-86.42
DLR	Del Rio, USA	29.49	259.08	38.87	-34.04
DMH	Danmarkshavn, Greenland	76.77	341.37	77.15	85.12
DOU	Dourbes, Belgium	50.1	4.6	45.79	81.68
DRV	Dumont d'Urville, Antarctica	-66.67	140.01	-80.65	-124.47
DRW	Darwin, Australia	-12.4	130.9	-21.53	-156.74
ESK	Eskdalemuir, Scotland, UK	55.32	356.8	52.65	77.41
EWA	Ewa Beach, Hawaii, USA	21.32	202	21.43	-90.00
EYR	Eyrewell, New Zealand	-43.4	172.4	-50.13	-103.35
FCC	Fort Churchill, Canada	58.76	265.92	69.04	-28.23
FHB	Paamiut, Greenland	62	310.32	67.63	39.03
FMC	Fort McMurray, Canada	56.66	248.79	64.29	-51.11
FRD	Fredericksburg, USA	38.2	282.63	49.08	-2.14
FRN	Fresno, USA	37.1	240.3	43.05	-56.30
FSP	Fort Simpson, Canada	61.76	238.77	67.34	-66.07

Table 1
Continued

IAGA code	Location	Geodetic latitude (°N)	Geodetic longitude (°E)	Mean corrected geomagnetic latitude (°N)	Mean corrected geomagnetic longitude (°E)
FUR	Fürstenfeldbruck, Germany	48.17	11.28	43.33	86.85
FYU	Fort Yukon, Canada	66.57	214.7	67.28	-93.86
GDH	Qeqertarsuaq, Greenland	69.25	306.47	75.79	40.39
GHB	Nuuk, Greenland	64.17	308.27	70.18	37.83
GIM	Gillam, Canada	56.38	265.36	66.24	-27.15
GLN	Glenlea, Canada	49.65	262.88	60.06	-31.75
GNA	Gnangara, Australia	-31.8	116	-43.98	-172.78
GUA	Guam	13.59	144.87	5.96	-144.13
GUI	Güímar, Canary Is.	28.32	343.57	12.91	60.66
HAD	Hartland, England, UK	50.98	355.52	47.55	74.87
HBK	Hartebeesthoek, S. Africa	-25.88	27.71	-36.09	94.69
HER	Hermanus, S. Africa	-34.43	19.23	-42.31	82.28
HLP	Hel, Poland	54.61	18.82	50.74	94.98
HON	Honolulu, Hawaii, USA	21.32	202	21.50	-90.13
HRB	Hurbanovo, Slovakia	47.86	18.19	43.03	92.69
HRN	Hornsund, Svalbard	77	15.6	74.18	108.69
HTY	Hatizyo, Japan	33.12	139.8	25.90	-148.91
IQA	Iqaluit, Canada	63.75	291.48	72.32	15.00
IRT	Irkoutsk, Russia	52.17	104.45	47.58	177.74
KAG	Kagoshima, Japan	31.48	130.72	24.80	-157.02
KAK	Kakioka, Japan	36.23	140.18	29.13	-148.35
KDU	Kakadu, Australia	-12.69	132.47	-21.78	-155.03
KNY	Kanoya, Japan	31.42	130.88	24.64	-157.04
KUV	Kullorsuaq, Greenland	74.57	302.82	80.81	42.87
LER	Lerwick, Scotland, UK	60.13	358.82	57.97	81.13
LOV	Lovoe, Sweden	59.35	17.83	55.85	96.36
LRM	Learmonth, Australia	-22.22	114.1	-33.09	-174.14
LRV	Leirvogur, Iceland	64.18	338.3	65.02	67.19
LYR	Longyearbyen, Svalbard	78.2	15.83	75.34	110.77
MAB	Manhay, Belgium	50.3	5.68	46.00	82.63
MAW	Mawson Station, Antarctica	-67.61	62.88	-70.35	90.48
MCM	McMurdo Station, Antarctica	-77.85	166.67	-79.91	-31.86
MCQ	Macquarie Island	-54.5	158.95	-64.34	-111.60
MEA	Meanook, Canada	54.62	246.65	62.12	-54.58
MGD	Magadan, Russia	59.97	150.86	53.89	-140.23
MMB	Memambetsu, Japan	43.91	144.19	37.04	-144.39
MSR	Moshiri, Japan	44.37	142.27	37.65	-145.93
MUT	Muntinlupa, Philippines	14.37	121.02	6.87	-167.21
NAL	Ny Ålesund, Svalbard	78.92	11.95	76.27	109.73
NAQ	Narsarsuaq, Greenland	61.16	314.56	66.20	43.47
NCK	Nagyecenk, Hungary	47.63	16.72	42.72	91.38
NEW	Newport, USA	48.27	242.88	54.94	-56.65
NGK	Niemegk, Germany	52.07	12.68	47.94	89.00

Table 1
Continued

IAGA code	Location	Geodetic latitude (°N)	Geodetic longitude (°E)	Mean corrected geomagnetic latitude (°N)	Mean corrected geomagnetic longitude (°E)
NUR	Nurmijärvi, Finland	60.5	24.65	56.96	102.10
ONW	Onagawa, Japan	38.43	141.47	31.52	-146.75
OTT	Ottawa, Canada	45.4	284.45	56.13	0.83
PAF	Port-aux-Français, Kerguelen Is	-49.35	70.26	-58.51	122.00
PBQ	Poste-de-la-Baleine, Canada	55.28	282.26	66.00	-1.68
PGC	Pangnirtung, Canada	66.1	294.2	74.14	20.10
PHU	Phú Thủy, Vietnam	21.03	105.95	14.31	178.11
PIN	Pinawa, Canada	50.2	263.96	60.15	-28.46
PPT	Pamatai, Tahiti	-17.57	210.42	-16.52	-74.68
PST	Port Stanley, Falkland Is	-51.7	302.11	-38.48	10.59
RAL	Rabbit Lake, Canada	58.22	256.32	67.01	-41.19
RAN	Rankine Inlet, Canada	62.82	267.89	72.47	-24.22
RES	Resolute Bay, Canada	74.69	265.11	83.38	-41.05
SBA	Scott Base, Antarctica	-77.85	166.78	-79.90	-31.99
SCO	Ittoqqortoormiit, Greenland	70.48	338.03	71.50	72.09
SIT	Sitka, Alaska, USA	57.07	224.67	59.76	-80.12
SJG	San Juan, Puerto Rico	18.11	293.85	28.09	10.31
SKT	Maniitsoq, Greenland	65.42	307.1	71.59	37.19
SMI	Fort Smith, Canada	60.02	248.05	67.43	-53.48
SOD	Sodankylä, Finland	67.37	26.63	63.90	107.45
SOR	Sørøya, Norway	70.54	22.22	67.46	105.71
SPA	South Pole Station, Antarctica	-90	-	-73.95	18.61
SPT	San Pablo Toledo, Spain	39.55	355.65	32.08	71.89
STF	Kangerlussuaq, Greenland	67.02	309.28	72.76	40.95
STJ	St Johns, Canada	47.6	307.32	53.87	31.30
SVS	Savissivik, Greenland	76.02	294.9	83.22	34.23
TAL	Taloyoak, Canada	69.54	266.45	78.56	-29.33
THL	Qaanaaq, Greenland	77.47	290.77	85.33	33.59
THY	Tihany, Hungary	46.9	17.54	41.86	91.97
TIK	Tixie, Russia	71.58	129	66.15	-162.08
TRO	Tromsø, Norway	69.66	18.94	66.69	102.68
TRW	Trelew, Argentina	-43.25	294.68	-29.91	4.99
TSU	Tsumeb, Namibia	-19.22	17.7	-30.14	87.12
TUC	Tucson, USA	32.17	249.27	39.77	-45.36
UMQ	Uummannaq, Greenland	70.68	307.87	76.46	42.84
UPN	Upernavik, Greenland	72.78	303.85	79.03	40.68
VAL	Valentia, Ireland	51.93	349.75	49.19	70.39
VIC	Victoria, Canada	48.52	236.58	53.85	-64.08
WNG	Wingst, Germany	53.75	9.07	50.00	86.77
YKC	Yellowknife, Canada	62.48	245.52	69.50	-59.40

Note. Mean corrected geomagnetic latitudes and longitudes are averages over all years for which 1-min cadence data were available at that site, computed using the International Geomagnetic Reference Field model. Sites in bold provided 1-s resolution data for this study.

as a further check, all data in weeks containing R_1 peaks above the 99.97th percentile ($P_{99.97}$) were visually inspected and obvious artifacts (such as large spikes, step changes, and instrument saturation effects) were replaced by data gaps, as described in Rogers et al. (2020).

At each magnetometer, the “ramp” change in the horizontal component of \mathbf{B} over n -minute intervals was defined as

$$\mathbf{R}_n = \{R_n(i); i = 1, 2, 3, \dots, k\} \quad (1)$$

$$R_n(i) = \sqrt{\left(\frac{B_N(i) - B_N(i-n)}{n\Delta t}\right)^2 + \left(\frac{B_E(i) - B_E(i-n)}{n\Delta t}\right)^2} \quad (2)$$

where k is the number of field measurements and $\Delta t = 1$ min was the cadence of the measurements. For computational efficiency, the n -minute backward difference values, \mathbf{R}_n , were calculated using n -point moving-average filters on the 1-min first differences of B_N and B_E . Intervals containing missing data were excluded from the analysis. The statistics of \mathbf{R}_1 (1-min field fluctuations) were modeled in Rogers et al. (2020). The definition in Equation 2 ensures that statistics of the induced E-field magnitude, $|E| = \sqrt{E_N^2 + E_E^2}$ will be approximately proportional to R_n (with exact proportionality for an idealized half-space model of surface conductivity—see Appendix A). The expression for R_1 is the same as that adopted by Freeman et al. (2019), Smith et al. (2019), Wintoft et al. (2015, 2016), Ngwira et al. (2018), Falayi et al. (2017), Kozyreva et al. (2018) and others, but differs slightly from the first differences of B_h (i.e., $d|B_h|/dt$) computed by some authors (e.g., Love, Coisson, & Pulkkinen, 2016; Thomson et al., 2011) particularly when there is a rapid change in the field direction.

The root-mean-square of \mathbf{R}_1 over n -minute periods was defined as

$$\mathbf{S}_n = \{S_n(i), i = 1, 2, 3, \dots, k\} \quad (3)$$

with

$$S_n(i) = \sqrt{\frac{1}{n} \sum_{j=i-n+1}^i R_1(j)^2} \quad (4)$$

and this was implemented in software using a convolution filter. Since we are only interested in extreme values, a high threshold for \mathbf{R}_n and \mathbf{S}_n was set at the 99.97th percentile level, $P_{99.97}$. The application of extreme value statistics (Coles, 2001) requires an assumption that exceedances of this threshold are temporally independent rather than clustered together. Therefore, the threshold exceedances were declustered to ensure a minimum 12 hr between clusters and only the peak value in each cluster was recorded. The MLTs (Laundal & Richmond, 2017) associated with each peak were also calculated as described by Rogers et al. (2020). Declustered exceedances ($\mathbf{R}_n > P_{99.97}$) were then fitted to a generalized Pareto (GP) “tail” distribution and the fitted GP profile was used to predict RLs expected over RPs of up to 500 years (see Coles, 2001; Rogers et al., 2020 for mathematical details). The analysis of extreme field fluctuations at 28 European magnetometer sites by Thomson et al. (2011) showed that the choice of a $P_{99.97}$ threshold and 12-hr declustering provides relatively stable GP coefficients while ensuring temporal independence of the extreme events. For consistency of approach, we have therefore adopted these thresholds for our analysis of magnetometer data worldwide.

A further set of magnetometer measurements at 1-s cadence were obtained for three sites in the United Kingdom operated by the British Geological Survey, namely, HAD (Hartland, southern England, and CG latitude $\lambda = 47.55^\circ$), ESK (Eskdalemuir, southern Scotland, $\lambda = 52.65^\circ$), and LER (Lerwick, Shetland Is, northern Scotland, $\lambda = 57.97^\circ$) (see Table 1). Data at 1-s resolution were available from January 1, 2001 to September 14, 2016 for all three sites, while the 1-min SuperMAG data set extended from January 1, 1983 to December 31, 2016 for all three sites. The data were visually inspected for weeks containing 1-s $|dB_h/dt|$ ($R_{1/60}$) exceeding the 99.97th percentile, and obvious artifacts removed in the same manner as for the 1-min

SuperMAG data set described above. When fitting GP distributions to predict RLs for the 1-s data sets, and for all averaging periods, $\tau \equiv n \Delta t$, we have used the same consistent percentile threshold (99.97th percentile) and declustering run-length (12-hr) as selected in the study of 1-min cadence measurements by Thomson et al. (2011) using a selection of visual diagnostics. Thomson et al. (2011) noted that, for most geomagnetic observatories in their study, the RL was “only weakly dependent on the decluster length.” Historically, in extreme value statistical analyses, justification of the threshold selected has been through visual diagnostics combined with any available scientific insight or expert knowledge on the process of interest. The use of visual diagnostics becomes infeasible as the number of data sets (in this case site-frequency combinations) grows. Consequently, we took a pragmatic approach and defined the same proportion of observations to be the tail sample for each site and for each value of τ . For a given τ , this permits a comparison of RLs across sites, and for a given site, it permits a comparison across all values of τ . As the duration of the 1-s data sets obtained from the UK observatory sites differed from those in the 1-min data set in the SuperMAG archive, we ran additional visual diagnostic checks for thresholds at 99.95, 99.97, and 99.99 percentiles (with and without 12-hr declustering applied) as were performed in the analysis by Thomson et al. (2011). These checks confirmed that for the $\Delta t = 1$ s data set, 12-hr declustering and the 99.97th percentile threshold remained the most appropriate for RL estimation at all three UK observatories.

The measurement of the ground magnetic field has a long established tradition in many countries and data quality and standards are set to a high level, for example, through INTERMAGNET (Love & Chulliat, 2013; Thomson & Flower, 2021). In contrast, long-term observations of the ground electric field are relatively rare (Beggan et al., 2021 and references therein) and more influenced by man-made electromagnetic noise due to a low signal-noise ratio. Available data sets are scarce and often discontinuous. In the United Kingdom, the ground electric field has been monitored at the three geomagnetic observatories (HAD, ESK, and LER) since 2015 with nonpolarizable electrodes along north-south (N-S) and east-west (E-W) oriented baselines (Some recent examples of these measurements are available online: http://www.geomag.bgs.ac.uk/data_service/space_weather/geoelectric.html).

To obtain estimates of the geoelectric field for times when no data were recorded, the horizontal geoelectric field spectrum, $\mathbf{E}(f) = \begin{pmatrix} E_x \\ E_y \end{pmatrix}$ may be estimated from the horizontal magnetic field spectrum $\mathbf{B}(f) = \begin{pmatrix} B_x \\ B_y \end{pmatrix}$ via

$$\mathbf{E}(f) = \mathbf{Z}(f)\mathbf{B}(f) / \mu \quad (5)$$

where μ is the permeability, and $\mathbf{Z}(f) = \begin{pmatrix} Z_{xx} & Z_{xy} \\ Z_{yx} & Z_{yy} \end{pmatrix}$ is the impedance (with units of Ω), where x and y refer to north and east components, respectively (e.g., Chave & Jones, 2012; Simpson & Bahr, 2005). Fourier transforms may be used to convert between the frequency (f) and time domains. The frequency-dependent term \mathbf{Z}/μ is called the MT transfer function (with units of V/km/nT) and is informative of the electrical conductivity structure of the subsurface that is useful in deep geophysical exploration.

\mathbf{Z}/μ was estimated from simultaneous measurements of the horizontal components of the ground electric and magnetic field using robust statistical approaches to minimize the influence of noise. For the estimation of \mathbf{Z}/μ at HAD, ESK, and LER, we used 6 months of electric and magnetic field measurements from 2015 and applied the impedance estimation algorithm of Smirnov (2003). Further details of the procedure are given in Beggan et al. (2021). Due to the sampling cadence of 1 s and the frequency response of the fluxgate magnetometers at the observatory sites, the impedance estimates cover a period range of 20–20,000 s (or 5×10^{-2} – 5×10^{-5} Hz).

3. Latitude, MLT, and Seasonal Distribution of Large R_n and S_n on Timescales From 1 to 60 min

Figure 1 presents the 99.97th percentiles of (a) Ramp changes (R_n) and (b) RMS fluctuations (S_n) at four sampling intervals, $\tau \equiv n \Delta t = 1, 10, 30,$ and 60 min, plotted against the mean absolute CG latitude, $|\lambda|$. Each point in the graphs represents $P_{99.97}$ at an individual magnetometer site, and the solid curves are smoothed spline fits to the data.

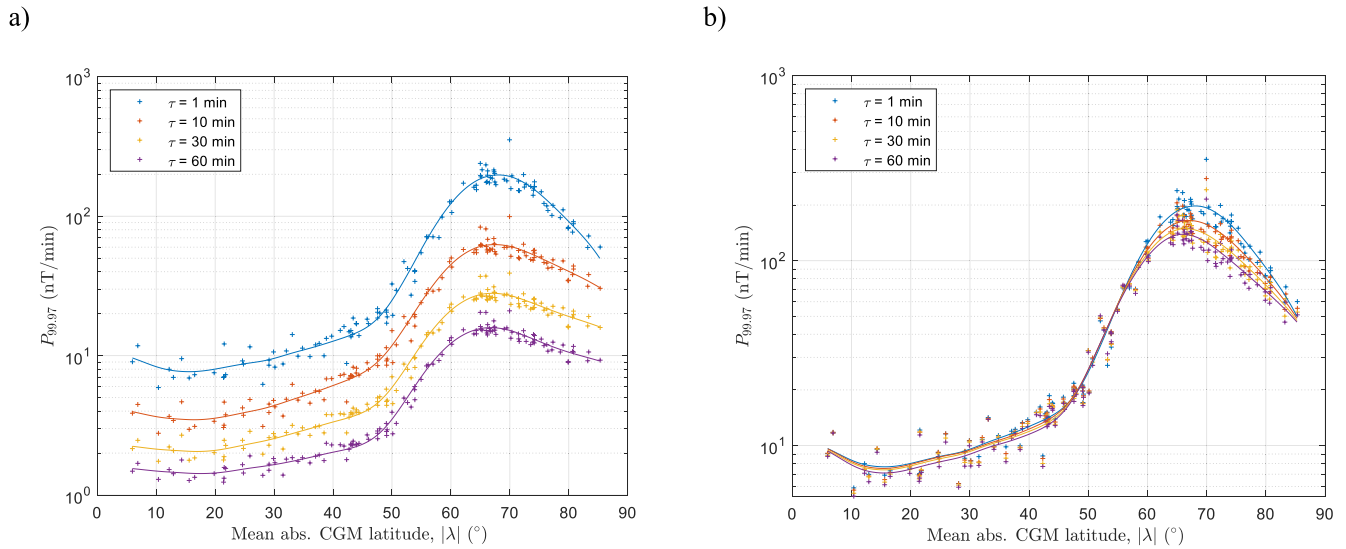


Figure 1. 99.97th percentiles of (a) ramp changes (R_1 , R_{10} , R_{30} , and R_{60}) and (b) a root-mean-square variations (S_1 , S_{10} , S_{30} , and S_{60}). Solid lines are smoothed spline fits.

The shapes of the profiles $P_{99.97}(|\lambda|)$ are broadly similar for both R_n and S_n and for all τ , consisting of a broad maximum centered about $|\lambda| \cong 67^\circ$, indicative of intense auroral current systems in this region, tapering to a minimum at $|\lambda| \cong 15^\circ$ with a slight increase toward the equator. The latter is indicative of stronger disturbances near the equatorial electrojets, a narrow band of enhanced ionospheric E -layer currents in the region $|\lambda| < 5^\circ$, which have previously been associated with elevated $|dB_h/dt|$ and GIC magnitudes (Adebesin et al., 2016; Carter et al., 2015; Ngwira et al., 2013; Pulkkinen et al., 2012). For ramp changes (Figure 1a), there is a strong dependence on τ and the shape of $P_{99.97}(|\lambda|)$ changes with τ (most clearly evident when comparing the curves for $\tau = 1$ and 10 min). The dependence of the RMS magnitude on τ (Figure 1b) is, to a first approximation, flat except at latitudes above $|\lambda| \cong 60^\circ$ where $P_{99.97}$ decreases with increasing τ . In Section 4, we shall further develop models of $P_{99.97}(|\lambda|, \tau)$ for both R_n and S_n and present similar models for their 100-year RLs.

To gain a better understanding of the physical drivers of these large fluctuations, we first examine their MLT dependence. Figure 2 presents the probability of (declustered) peaks of $|dB_h/dt|$ exceeding $P_{99.97}$ as a function of $|\lambda|$ and MLT. This was calculated by counting the number of peaks in 1-hr bins of MLT and 3.3° bins of $|\lambda|$, where data from multiple magnetometers were aggregated where they lay within the same latitude bin. (Bin sizes were chosen as a compromise between resolution and quantization noise). The bin counts were then normalized by the total number of field measurements in each bin. Panels (a–d) present the distributions for ramp changes over 1, 10, 30, and 60 min, respectively, while panels (e–h) present the distributions for the RMS magnitudes over 1, 10, 30, and 60 min, respectively. We have used absolute latitude on the vertical axes since the distributions of occurrence probability against (signed λ , MLT) were, to a close approximation, symmetric about $\lambda = 0$. Note that panels (a and e) are identical, which may be noted from Equation 4 with $n = 1$. When interpreting the distributions in Figure 2, it is important to remember that the threshold $P_{99.97}$ itself varies with $|\lambda|$ (see Figure 1) and as such it is simplest to focus on the MLT distribution in each individual latitude band. It is also important to note that, due to the method of declustering, peaks occurring within 12-hr of a larger peak are not represented. However, it was observed that if the peaks over threshold were not declustered, then the general shape and form of the probability distribution in Figure 2 remained largely unaltered; for $|\lambda| > 40^\circ$, with no declustering, the occurrence probabilities were slightly reduced in the hours 12–24 MLT and slightly raised in the hours 0–12 MLT, indicating a greater clustering of peaks associated with events occurring prenoon.

At the highest latitudes ($|\lambda| > 80^\circ$), poleward of the dayside cusp, there is an occurrence maximum in the few hours about noon MLT, which persists over all timescales (1–60 min). For $\tau > 1$ min, the maximum is

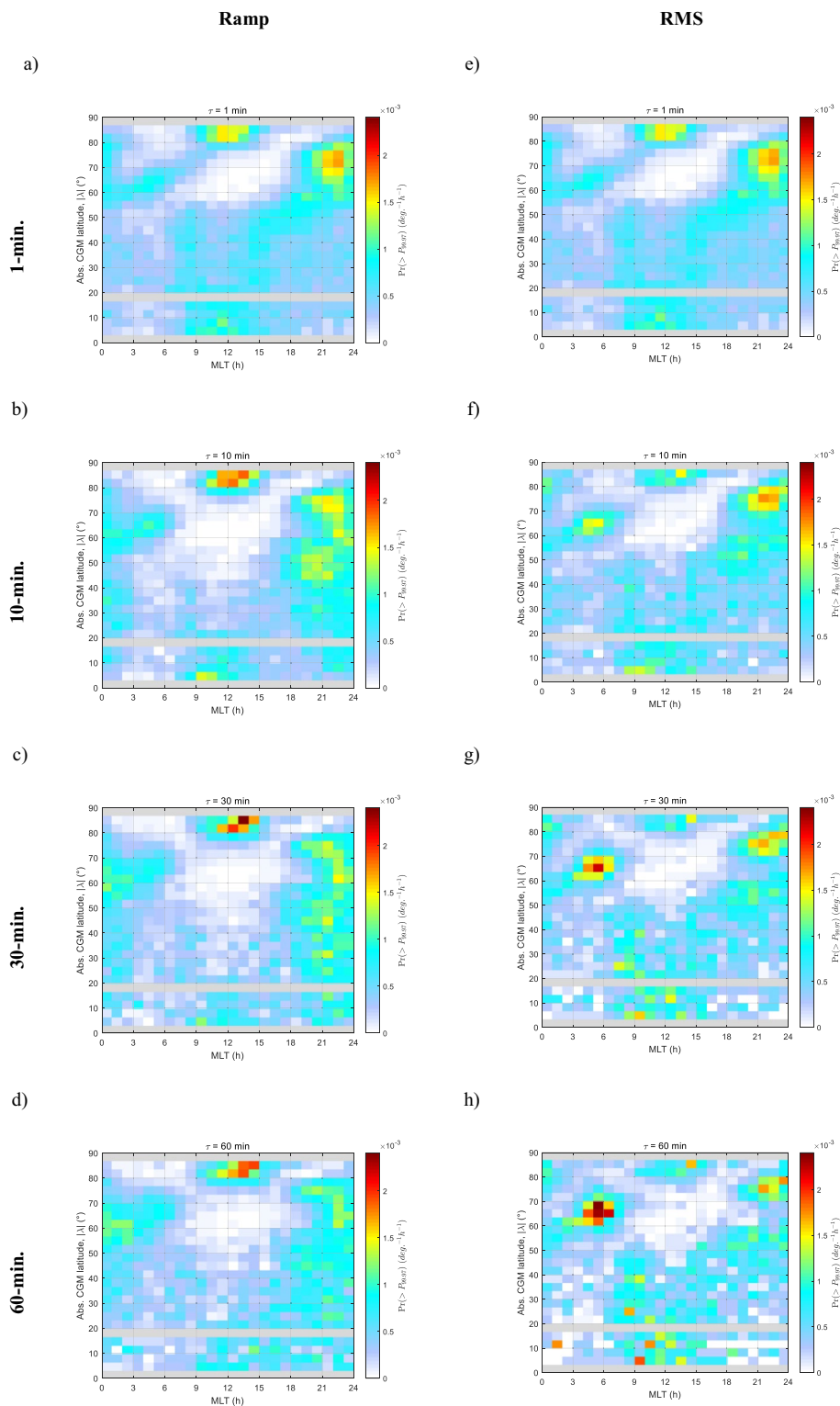


Figure 2. $\Pr(|dB_h/dt| > P_{99,97})$ against corrected geomagnetic latitude and magnetic local time (MLT) for (a) R_1 , (b) R_{10} , (c) R_{30} , (d) R_{60} , (e) $S_1(=R_1)$, (f) S_{10} , (g) S_{30} , and (h) S_{60} . Latitude bins with no magnetometers are colored gray.

much more sharply peaked for ramp changes than for RMS fluctuations, and as τ increases toward 60 min, the MLT of the maximum occurs slightly later (toward 14 MLT). (Note that the timestamps and MLTs associated with each cluster peak of $|dB_n / dt|$ refers to the *end* of the n -minute period in question (from Equations 2 and 4) but this is not sufficient to account for the apparent shift of the maximum toward post-noon.) Analysis of the R_1 distribution by Rogers et al. (2020) showed that these peaks near noon occur predominantly under northward IMF conditions during the summer months (i.e., under conditions of greatest dipole tilt angle), suggesting a possible relation to impulsive field line reconnection between the IMF and an “overdraped” tail lobe (Crooker, 1992; Milan et al., 2017, 2020; Wang et al., 2008; Watanabe et al., 2005). The MLT distribution of occurrence probability at dayside cusp latitudes does not match the distributions of MIEs observed by Lanzerotti et al. (1991) and Kataoka et al. (2003) who reported a relatively flat distribution over 06–18 MLT with a minimum around 11 MLT, although these MIE distributions were not thresholded at a very high percentile. Nonetheless, the MIE amplitude distribution presented in Figure 5d of Kataoka et al. (2003) indicates perturbations approaching 400 nT (over ~5–15 min) in the 07–11 MLT period, which is not observed in the MLT profile of $P_{99,97}$ exceedances of Figure 2a. Such discrepancies indicate that it is less likely that MIEs (caused by TCVs) provide a significant contribution to the extremes of $|dB_n / dt|$ in this region.

At low latitudes $|\lambda| < 40^\circ$, for R_1 and R_{10} , and S_n for all n , the occurrence probabilities increase on the day-side at 07–16 MLT, although for $20^\circ < |\lambda| < 43^\circ$ the distribution is double-peaked with a dip in occurrence in the few hours around noon, creating a Y-shaped pattern most clearly discernible in the 1-min data (panels a or e). The distributions for R_{10} and R_{30} also have a nighttime maximum in the period (19–03 MLT). Rogers et al. (2020) showed (in their Figure 8) that ~25%–70% of the R_1 peaks at these latitudes occurred at or within 30 min of a sudden commencement, as recorded with high confidence in IAGA bulletins (<http://www.obsebre.es/en/rapid>). However, the lower figure (25%) was associated with the largest occurrence probabilities near noon, suggesting that alternative or delayed driving processes may be contributing to the largest R_1 at these times.

At auroral latitudes ($60^\circ < |\lambda| < 75^\circ$), the occurrence probability $Pr(R_n > P_{99,97})$, is greatest in the few hours before local midnight (20–24 MLT) for all timescales. Substorm onsets occur most frequently in this MLT sector (Liou et al., 2001; Wang et al., 2005) so the increased prevalence of large R_n may be associated with the substorm expansion and recovery phases themselves or with transient and localized MPEs, most of which occur within 30 min of a substorm onset. Engebretson et al. (2021) recently presented a statistical survey of MPEs at five Canadian sites (65–75°N geomagnetic) and their Figure 4 showed that the distributions of MPE above a threshold of 6 nT/s (360 nT/min) (with a maximum of 37 nT/s [2,220 nT/min]) contained a distribution in the range 02–06 MLT at only the lowest latitude station (65°N) while for the other four stations (71°N–75°N) a broad distribution of MPE occurrence was observed in the pre-midnight hours over 19–01 MLT. This observation is consistent with the MLT occurrence distributions shown in Figures 2a and 2b. The MLT of peak occurrence (in the pre-midnight hours) is ~1 hr earlier at the midlatitudes associated with UK magnetometers (HAD, ESK, and LER) ($\lambda = 47.5^\circ\text{N}$ – 58°N). Freeman et al. (2019) observed that, for the same three UK sites, ~55% of R_1 peaks exceeding $P_{99,97}$ were associated with the expansion or recovery phase of a substorm.

A secondary peak of occurrence is observed in the dawn-noon sector. Some of these peaks below 70°N may be associated with MPEs since they are consistent with the 02–06 MLT distribution observed by Engebretson et al. (2021) for the station at 65°N geomagnetic as noted above. However, this is also a region in which Pc5 pulsations are the dominant wave activity (e.g., Engebretson et al., 1998; Pulkkinen & Kataoka, 2006). The R_1 occurrence probabilities maximize at around 03 MLT at $|\lambda| = 60^\circ$, increasing to 12 MLT at $|\lambda| = 80^\circ$, and similar patterns have been reported in the distribution of Pc5 wave power (compare, for example, Figure 5 of Vennerström, 1999, Figures 2 and 4b of Baker et al., 2003, or Figure 1 of Weigel et al., 2002). The rate of occurrence for longer-period ramp changes, R_{10} , R_{30} , and R_{60} , is suppressed in the latitude band $|\lambda| = 70$ – 77° , although this may be an effect of declustering where the peaks occur within 12 hr of larger amplitude fluctuations in the pre-midnight sector.

In contrast to the distribution of ramp changes, the occurrence patterns of large RMS fluctuations (Figures 2e–2h) show that as the period τ increases, the probability of occurrence $Pr(S_n > P_{99,97})$ in the auroral zone increases strongly in the dawn sector (03–07 MLT). A cursory inspection of magnetograms for the

largest peaks of S_n indicated that many are indeed associated with ULF wave activity lasting tens of minutes (see, e.g., Figure 1c of Rogers et al., 2020). To examine this further, an analysis of the probability of occurrence versus (month, MLT) is presented in Figure 3 for the 26 sites at latitudes $\lambda = 60^\circ$ – 70° N. This figure shows that in the pre-midnight hours the frequency of occurrence is greatest near the equinoxes, when the geomagnetic field is more favorably oriented for reconnection with the IMF (Russell & McPherron, 1973; Zhao & Zong, 2012). However, for RMS fluctuations (Figures 3e–3h), as τ increases from 1 to 60 min, the greatest frequency of occurrence occurs on the dawn side (03–09 MLT). We also note, for both R_1 and S_1 distributions, a change in the locus of peak occurrence from 04–05 MLT near the summer solstice to 07–08 MLT near the winter solstice, which may be associated with changes in the position of the dawn terminator at these latitudes and the seasonal changes in the geometry of the geomagnetic field relative to the IMF. For $\tau \geq 10$ min, however, the frequency of occurrence in the winter months (December and January) is reduced relative to that for $\tau = 1$ min, in both R_n and S_n , and this also limits the time zones of occurrence in the late morning.

4. The Frequency and Latitude Dependence of R_n and S_n

4.1. Modeling the 99.97th Percentile

We now develop a model for the geomagnetic fluctuation amplitude as a function of sampling frequency and geomagnetic latitude, first for the 99.97th percentile of $|dB_n / dt|$ and in Section 4.2 for predicted 100-year RL estimates. Figure 4 presents $P_{99.97}$ as a function of sampling frequency, $f_s = 1/\tau$ for (a) R_n and (b) S_n at each of 125 magnetometer sites. The color of each line indicates the absolute CG latitude of the site, $|\lambda|$, and the upper horizontal scale indicates the sampling period, τ . Since the axes are logarithmic in both $P_{99.97}$ and f_s , a straight line with gradient p would indicate the power-law relation, $P_{99.97}(f_s) \propto f_s^p$, but it is clear from the curvature of the lines, at least for ramp changes, that this is not an appropriate model and it is observed that the gradients, curvature, and offset vary with latitude. This was modeled by fitting a quadratic function,

$$\mathbf{y} = p_1 \mathbf{x}^2 + p_2 \mathbf{x} + p_3 \quad (6)$$

where $\mathbf{y} = \log(P_{99.97}(f_s))$ and $\mathbf{x} = \log(f_s)$.

The best-fit quadratic coefficient, p_1 , linear coefficient, p_2 , and constant term, p_3 , are presented in Figure 5 as a function of $|\lambda|$. Here, the error bars are 95% confidence intervals (CIs). The distributions are approximately symmetric about the geomagnetic equator ($\lambda = 0$). We have fitted smoothing splines (solid curves) using the absolute CG latitude as the dependent variable (i.e., fitting to $p_k(|\lambda|)$, for $k = 1, 2$, and 3) and weighting each point by the inverse of the 95% CI. The constant terms (p_3) have broad maxima in the auroral zones as expected from Figure 1. However, for ramp changes (Figure 5a), the linear and quadratic coefficients (p_2 and p_1) also show a strong dependence on $|\lambda|$. For RMS fluctuations (Figure 5b), the changes in p_2 and p_1 are much less significant. The smoothing spline fits to the coefficients thus provide a global model for the 99.97th percentiles of R_n and S_n .

The goodness of the quadratic fits at each magnetometer site is presented in Figure 6 for 99.97th percentiles of R_n (left panels, a and b) and S_n (right panels, c and d). Panels (a and c) present the coefficients of determination, r^2 . To better illustrate values of r^2 close to 1, the vertical axis scaling in panels a and c is “inverse logarithmic” such that a set of values, $r^2 = 1 - 10^{-m}$ would be uniformly spaced for uniformly spaced m . Panels (b and d) present the RMS percentage error (i.e., the RMS value of $100\% \times (\hat{P}_{99.97} - P_{99.97}) / P_{99.97}$, where $\hat{P}_{99.97}$ are the model estimates). The quadratic models for R_n fit well, with $r^2 > 0.99$ for all sites (see panel a) and RMS residuals less than 3%. The quadratic model for S_n fits well at high latitudes ($|\lambda| > 60^\circ$), with $r^2 > 0.99$ (panel c), and for all sites the RMS of residuals is very low (<1.2%).

4.2. Modeling Return Levels

GP distribution functions were fitted to exceedances of R_n above a $P_{99.97}$ threshold (after 12-hr run-length declustering above the same threshold) independently for each magnetometer site. 100-year RLs of R_n were then determined from the GP distribution at a probability level equivalent to a 1-in-100 years of observa-

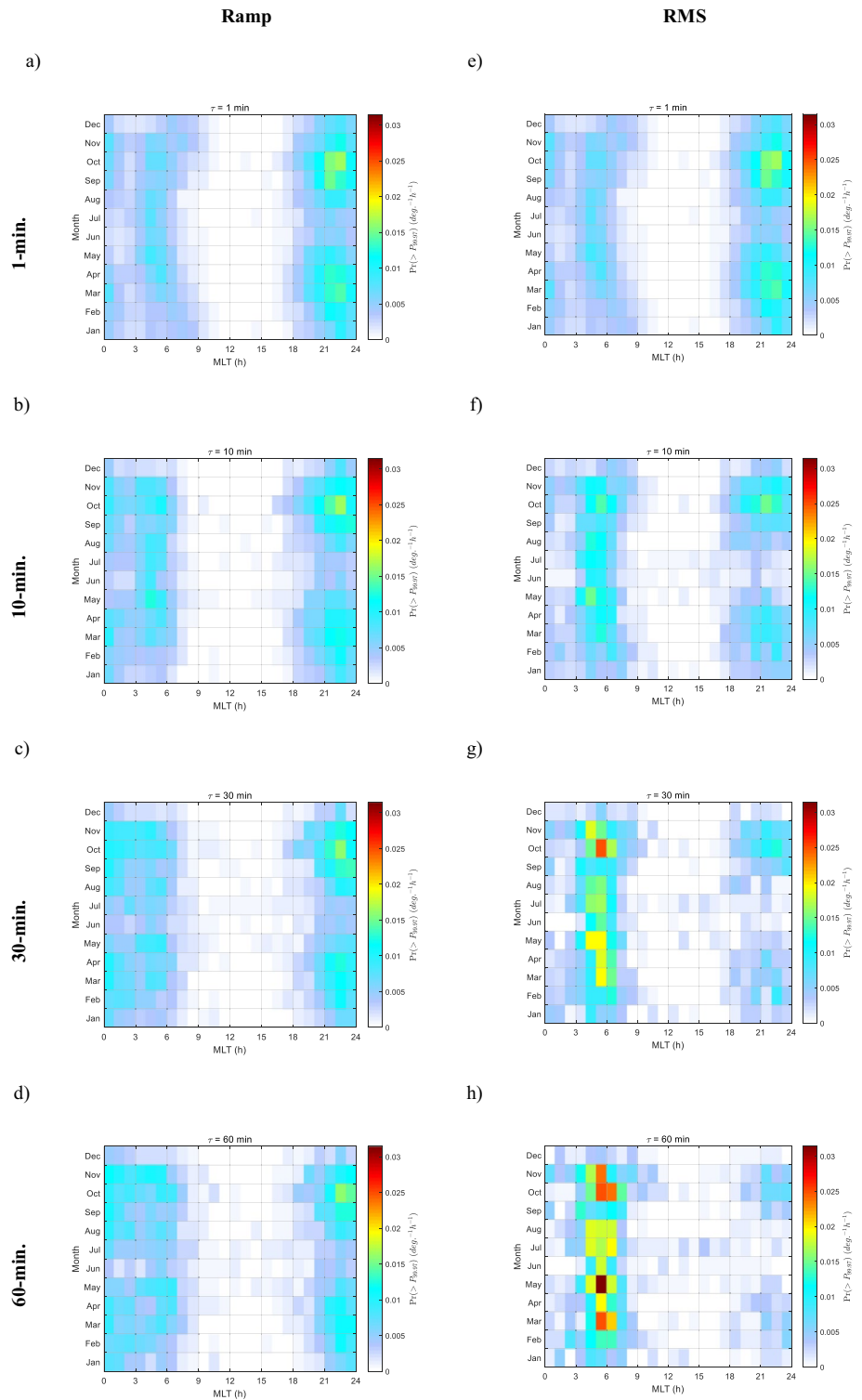


Figure 3. $Pr(|dB_h / dt| > P_{99,97})$ versus (magnetic local time [MLT], month) for (a) R_1 , (b) R_{10} , (c) R_{30} , (d) R_{60} , (e) $S_1(=R_1)$, (f) S_{10} , (g) S_{30} , and (h) S_{60} for stations between 60 and 70°N corrected geomagnetic latitude. RMS, root-mean-square.

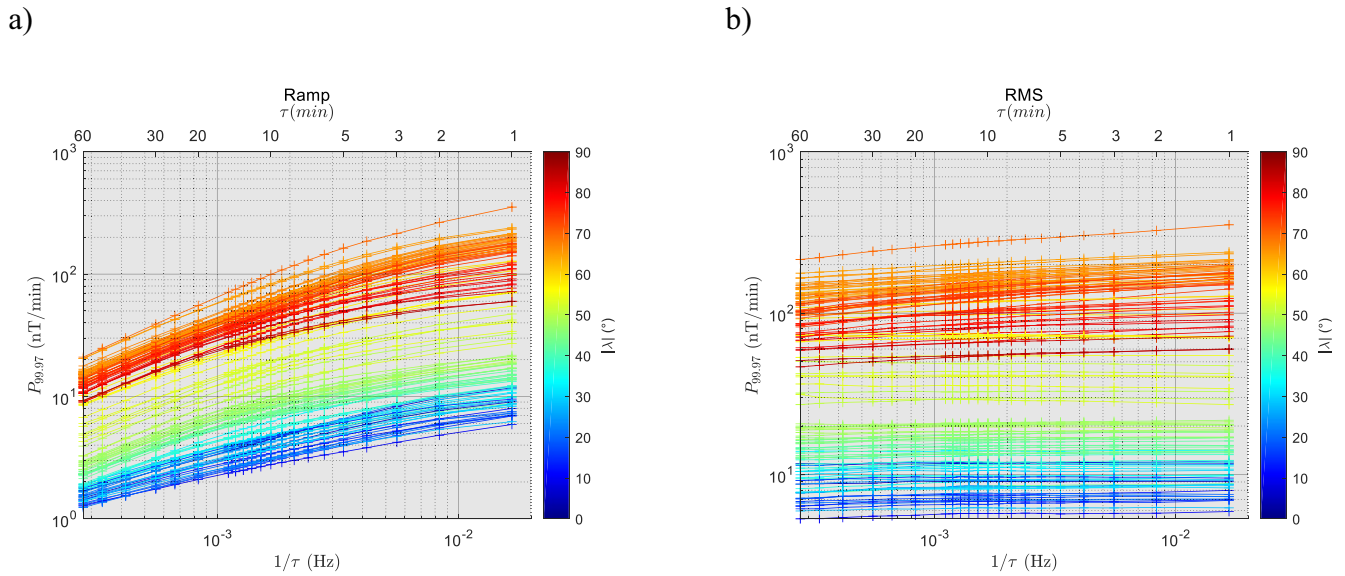


Figure 4. 99.97th percentiles of $|dB_h / dt|$ for (a) Ramp changes (R_n) and (b) root-mean-square (RMS) variation (S_n) for 125 magnetometers, as a function of sampling frequency, $f_s = 1/\tau$, and colored according to absolute corrected geomagnetic latitude, $|\lambda|$.

tions. A numerical method was used to determine a maximum likelihood estimate (MLE) for the RL with 95% confidence intervals determined from the (asymmetric) log-likelihood profile, as described in Gilleland and Katz (2016). This procedure was repeated for all 125 magnetometer sites and the results are plotted against $|\lambda|$ in Figure 7. Panels (a–d) present 100-year RLs of R_n for $n = 1, 10, 30,$ and 60 (min), respectively; points represent MLEs (colored blue for southern hemisphere sites, black for northern hemisphere) with error bars indicating the 95% CI. The red curve in each panel is a smoothing-spline interpolation to the MLE values. In Figure 8, the interpolating spline curves are presented for RPs from 5 to 500 years.

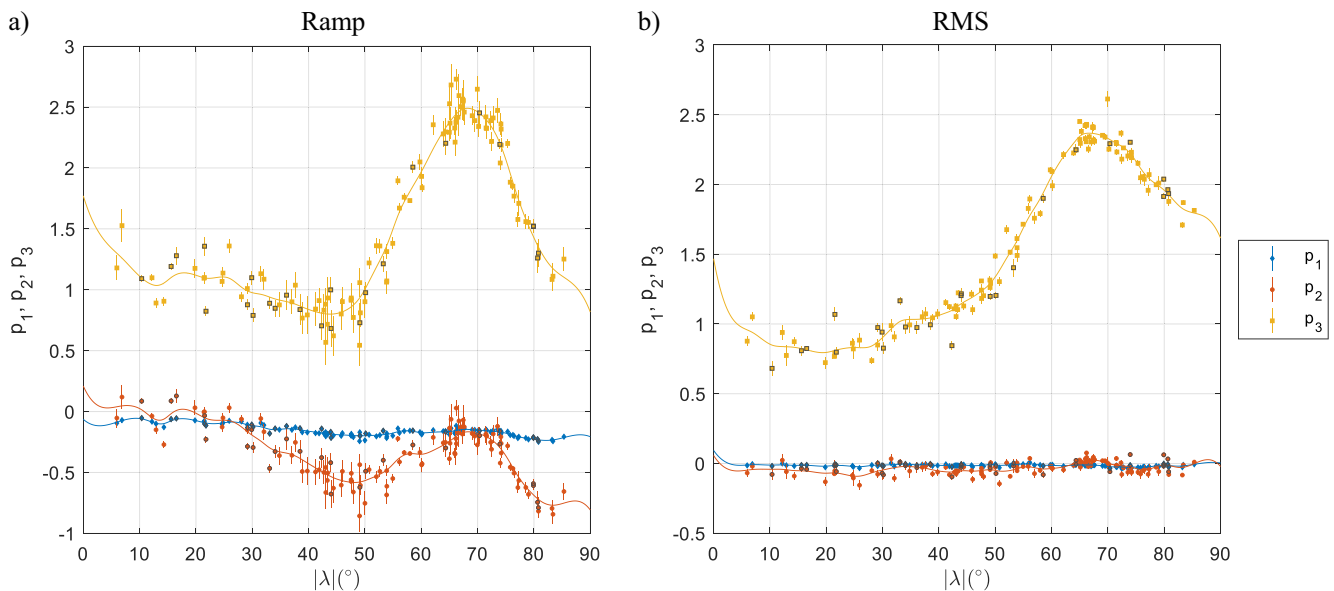


Figure 5. Coefficients of the polynomial (6) fitted to $\log P_{99.97}(\log f_s)$ at 125 magnetometers, for (a) R_n and (b) S_n as a function of absolute corrected geomagnetic latitude. Markers for Southern Hemisphere sites have a gray outline. Error bars indicate 95% confidence intervals (CIs). Solid lines indicate smoothed spline fits to $p_k(|\lambda|)$, for $k = 1, 2,$ and 3 with points weighted by $1/CI$. Units of p_k are $(10 \text{ dB nT min}^{-1} \text{ deg.}^{-k-3})$. RMS, root-mean-square.

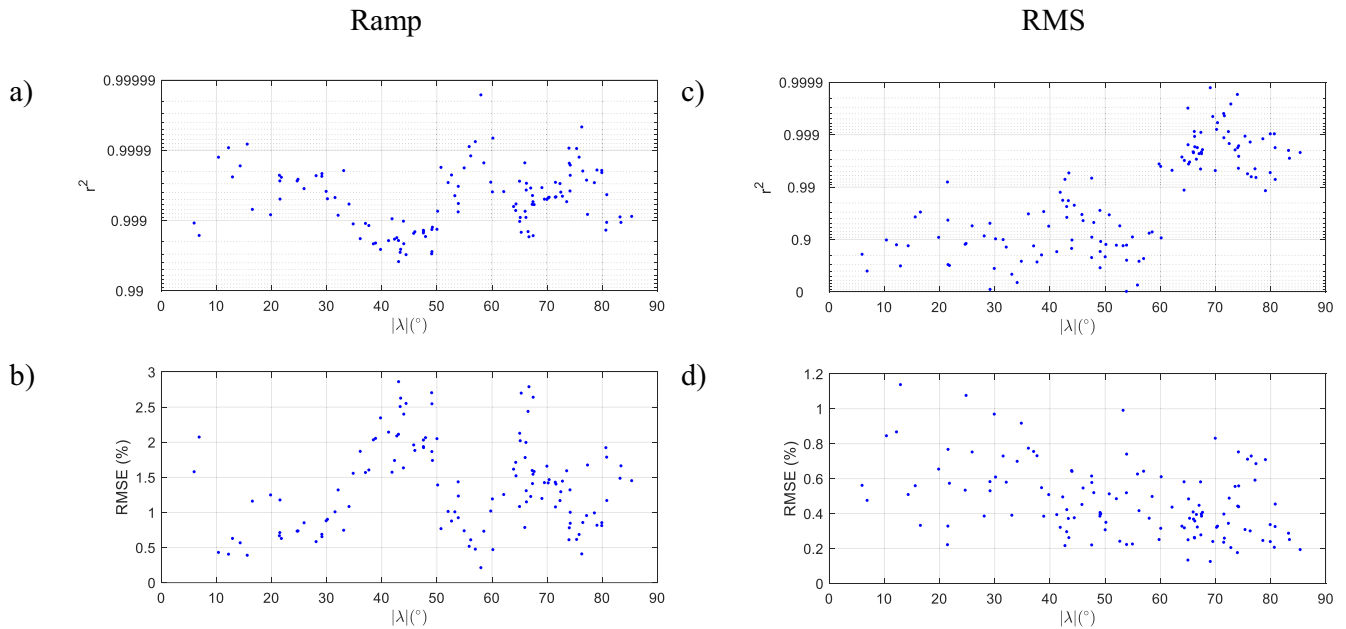


Figure 6. Goodness of fit metrics for the polynomial fit to $\log P_{99,97}(\log f_s)$ for (a and b) Ramp changes, and (c and d) root-mean-square (RMS) variations. Top panels (a and c) are coefficients of determination, r^2 . Bottom panels (b and d) are the RMS of residuals.

The 100-year RLs for R_1 (Figure 7a) (1-min ramp changes) are distinctly elevated for sites around $|\lambda| \cong 52\text{--}54^\circ$ and reference to Figure 8 indicates that the latitude of this maximum decreases with increasing RP. This indicates that the extreme R_1 events (declustered threshold exceedances) that occur less frequently (i.e., with longer RPs) have greater amplitude and occur at lower absolute latitudes. This pattern of behavior could indicate that largest and rarest auroral current fluctuations occur during substorm expansions associated with brightening auroral arcs at the equatorward edge of a greatly expanded auroral oval (i.e., following a large substorm growth phase). Over 10–60-min timescales (Figures 7b–7d), the peak near 53° is still present but less pronounced, and Figures 8b–8d show that it has similar or lower magnitude than the broad peak around $|\lambda| \cong 67^\circ$ that was observed in the $P_{99,97}$ profiles (Figure 1a).

The same procedure of fitting GP distribution functions was used to determine extreme values for the RMS variation over n -minute periods, S_n . Figure 9 presents the 100-year RLs and Figure 10 presents the smoothed-spline fits for 5–500-year RPs for the S_n , again for periods of $\tau = 1, 10, 30,$ and 60 min. The shape of these distributions is very similar to those of the R_n fluctuations although the reduction in level with increasing τ is much less pronounced.

For both R_n and S_n metrics (Figures 8 and 10, respectively), there is an increase in RLs toward the equator, potentially associated with activity in the equatorial electrojet current systems; and for RPs greater than 100 years, there is a predicted increase in RL as latitude $|\lambda|$ increases above 74° , for $\tau = 1$ and 10 min.

The RL predictions presented above should be interpreted with caution for RPs of 100 years or more (i.e., well in excess of the duration of measurements). Our analysis is based purely on the statistical temporal properties of measurements at individual magnetometer sites, and we have not attempted to model the spatial variation in the probability distributions. Magneto-hydrodynamic modeling (e.g., Ngwira et al., 2014) has indicated that the intense auroral electrojet currents that drive extreme values of R_n and S_n may, under extreme solar conditions, extend much further equatorward than suggested by our results, and historical records suggest that auroras during the September 1859 “Carrington” storm would have been observed at the zenith at geomagnetic latitude 31°N (Cliver & Dietrich, 2013). The measurements at low-latitude sites contain no observations of such extreme conditions and therefore may indicate misleadingly low RLs. Similar situations (in which more severe events tend to be spatially more localized) are frequently encountered in environmental and geospatial data sets and advanced methods for analyzing such “spatial extremes” are reviewed by Hüser and Wadsworth (2020).

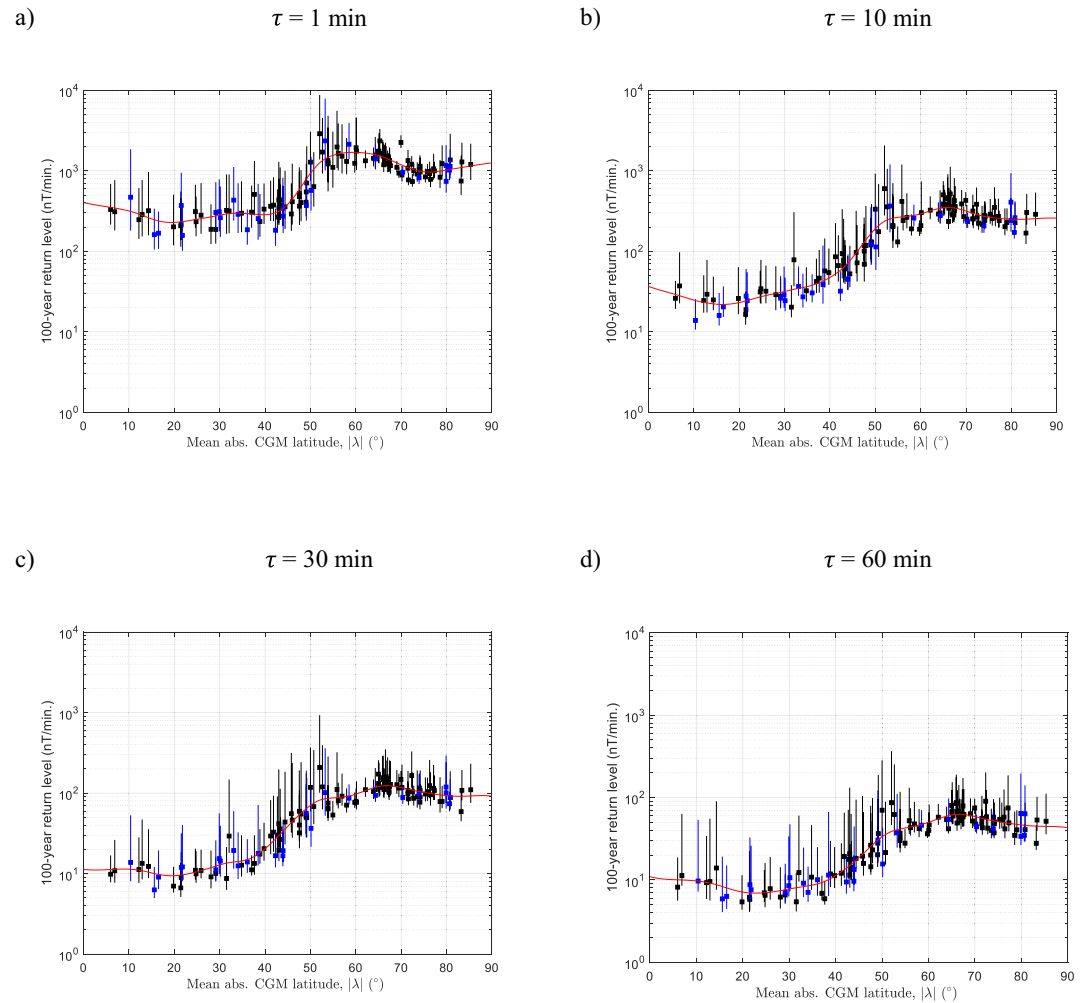


Figure 7. Hundred-year return levels (Max. likelihood estimates with 95% confidence interval shown as error bars) for ramp changes (R_n) estimated from generalized Pareto distributions fitted above $P_{99.97}$. Black indicates NH sites and blue indicates SH. (a) $\tau = 1$ min, (b) $\tau = 10$ min, (c) $\tau = 30$ min, and (d) $\tau = 60$ min. The red curves are smoothed spline fits to maximum likelihood estimates.

We now present models of the MLEs of 100-year RLs of R_n and S_n as functions of sampling frequency, f_s , and absolute CG latitude, $|\lambda|$, following the same procedure as for the $P_{99.97}$ levels developed in Section 4.1. Figure 11 presents 100-year RLs for (a) R_n and (b) S_n , in the same format as Figure 4. The coefficients of the polynomials (6) fitted to the RLs are presented in Figure 12. The 95% CI of the fitted coefficients (error bars in Figure 12) are larger than for the $P_{99.97}$ model, but the profiles remain approximately symmetric about $\lambda = 0^\circ$. It is interesting to note for the ramp changes, R_n , there is a pronounced change from positive to negative curvature as $|\lambda|$ increases, which can be seen in the profiles of Figure 11 and the change in quadratic coefficient, p_1 , in Figure 12. For both R_n and S_n , the gradients (or the linear coefficients, p_2) are significantly higher at lower latitude $|\lambda|$.

Figure 13 provides goodness of fit metrics for the polynomials (6) fitted to MLE of RL_{100} , presented in the same format as Figure 6. Not unexpectedly, RL_{100} shows greater variation from the polynomial model than $P_{99.97}$ (cf. Figure 6) but in the vast majority of cases the RMS errors are still less than 15% and have a coefficient of determination greater than 0.9.

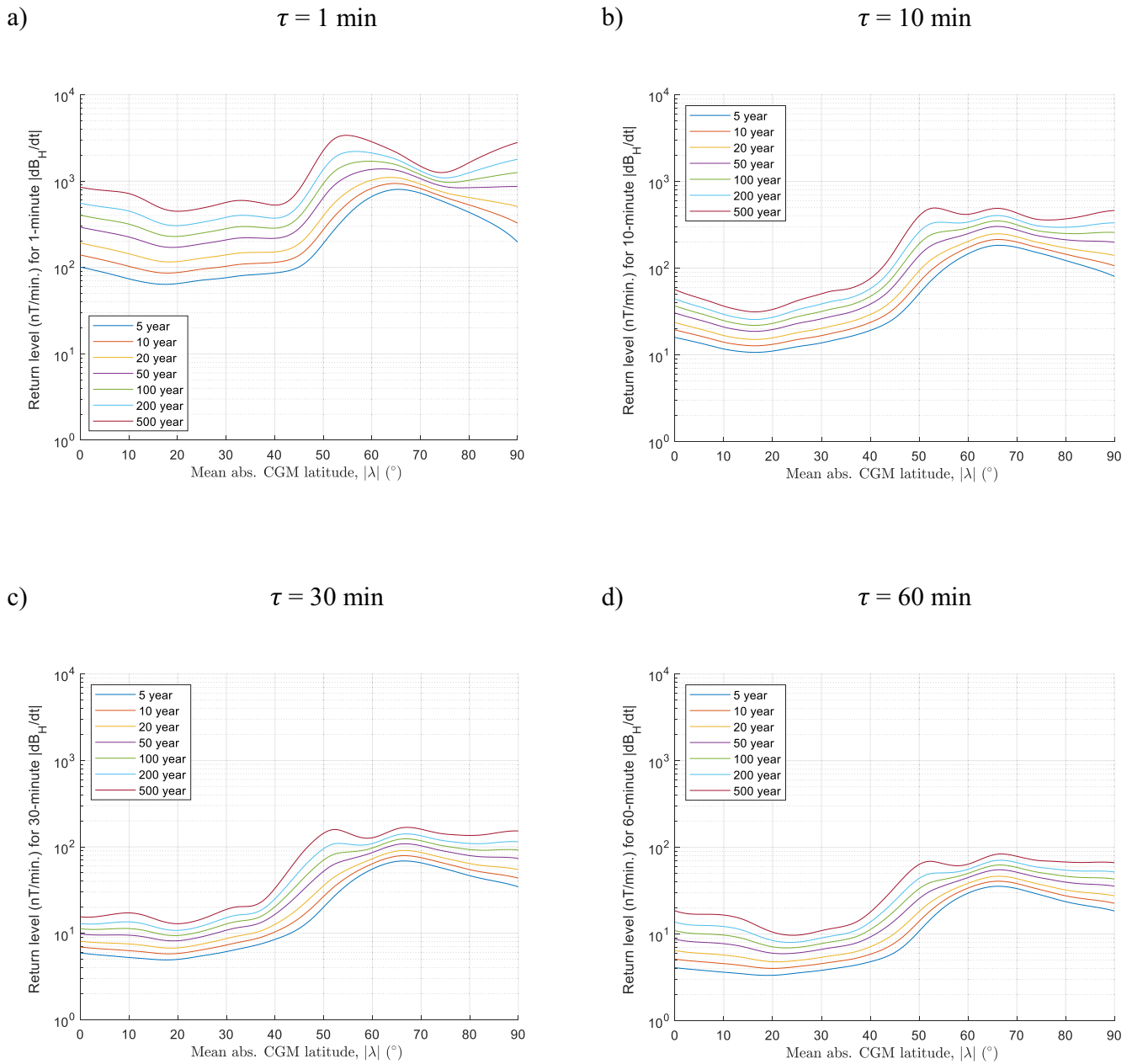


Figure 8. Smoothed spline fits to return levels of Ramp changes (R_n), as shown by the red curve in Figure 7 (100-year Return Period), but repeated for a range of return periods. (a) $\tau = 1$ min, (b) $\tau = 10$ min, (c) $\tau = 30$ min, and (d) $\tau = 60$ min.

4.3. Predictions of Extreme Geoelectric Fields in the United Kingdom

We shall now focus on the statistics for three UK magnetometer sites, HAD, ESK, and LER. Figure 14 presents for each site, the 99.97th percentiles of (a) R_n , (b) S_n , 100-year RLs for (c) R_n , and (d) S_n . For the ramp changes, R_n (Figures 14a and 14c) the frequency scale is extended up to 1 Hz using the 1-s cadence data set. While the length of the data sets differ for 1-s and 1-min data, the discontinuities in the $P_{99.97}$ curves (Figure 14a) at $\tau = 1$ min are negligible, although a larger discontinuity arises from the RL estimates (Figure 14c). Statistics for S_n (Figures 14b and 14d) could not be extended to 1 Hz since they are defined from 1-min cadence measurements (Equation 4), but they are presented here for $\tau = 1$ –60 min to illustrate that while the 99.97th percentile varies little with sample frequency (panel b), their 100-year RLs (panel d) have

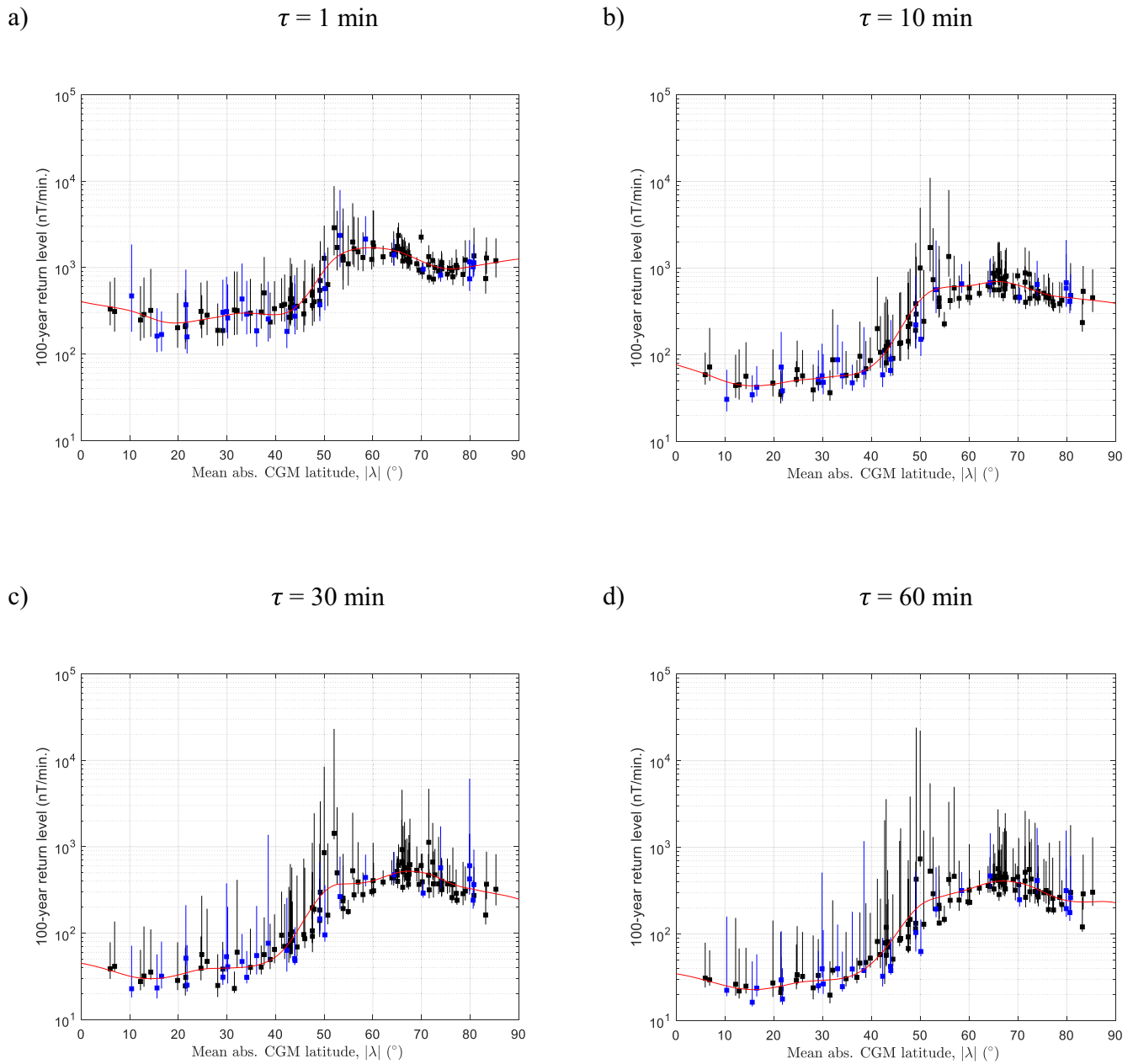


Figure 9. Hundred-year return levels (Max. likelihood estimates with 95% confidence interval shown as error bars) for root-mean-square variations (S_n). Black indicates NH sites and blue indicates SH. (a) $\tau = 1$ min, (b) $\tau = 10$ min, (c) $\tau = 30$ min, and (d) $\tau = 60$ min. The red curves are smoothed spline fits to maximum likelihood estimates.

a much more significant frequency dependence, albeit with large 95% confidence intervals (illustrated by the shaded regions).

To derive estimates of the $P_{99,97}$ and 100-year RLs of the geoelectric field from statistics of the geomagnetic field, we make use of the MT transfer functions, $\mathbf{Z}(f)/\mu$ measured at each UK site, as described in Section 2. In Figure 15 (panels a, c, and e), we present, for each site, the “apparent resistivity” associated with each of the four components of the observed \mathbf{Z}/μ , defined as

$$\rho_{a(ij)} = \frac{\mu_0}{2\pi f} \left| \frac{Z_{ij}}{\mu} \right|^2 \quad (7)$$

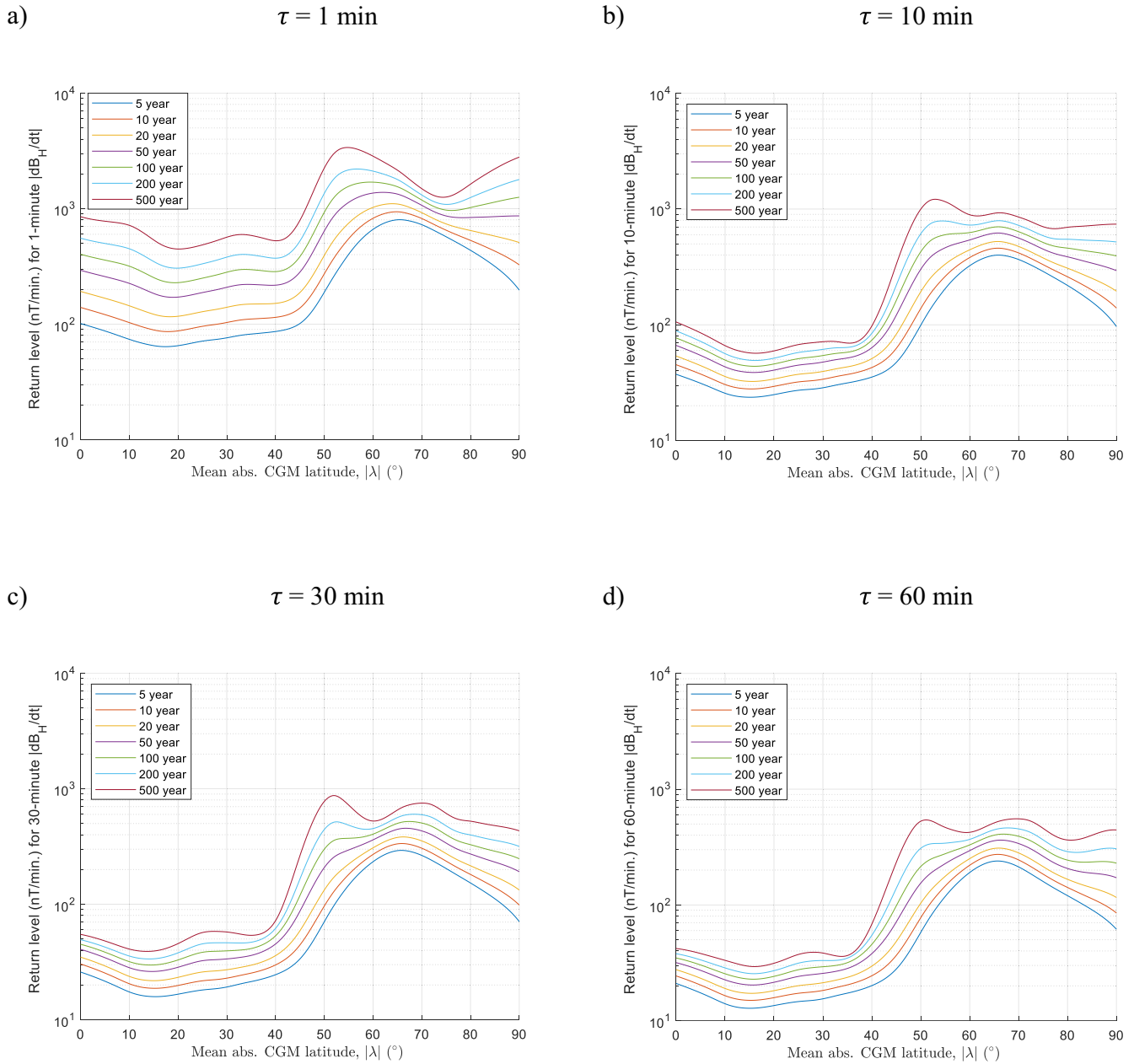


Figure 10. Smoothed spline fits to return levels of root-mean-square variation (S_r), as shown by the red curve in Figure 9 (100-year Return Period), but repeated for a range of return periods. (a) $\tau = 1$ min, (b) $\tau = 10$ min, (c) $\tau = 30$ min, and (d) $\tau = 60$ min.

where ($Z_{ij} = Z_{xx}, Z_{xy}, Z_{yx}, Z_{yy}$) are the components of the impedance matrix, \mathbf{Z} . Figure 15 panels (b, d, and f) show the phases of Z_{ij} . Apparent resistivity is the resistivity of an electrically homogeneous and isotropic half-space of permeability $\mu = \mu_0$ (the permeability of free space) that would be consistent with the measured \mathbf{E} and \mathbf{B} fields. Cagniard (1953) and Pirjola (1982) showed that using a simple half-space model of the surface, an electromagnetic wave polarized in the N-S plane, at the surface ($z = 0$), the magnetic field

$$B_N = B_0 e^{i(2\pi ft - kz)} = B_0 e^{i2\pi ft} \quad (8)$$

would induce a geoelectric field, E , at the surface ($z = 0$) of

$$E_E = -\sqrt{\frac{2\pi f}{\mu_0 \sigma}} B_N e^{i\pi/4} \quad (9)$$

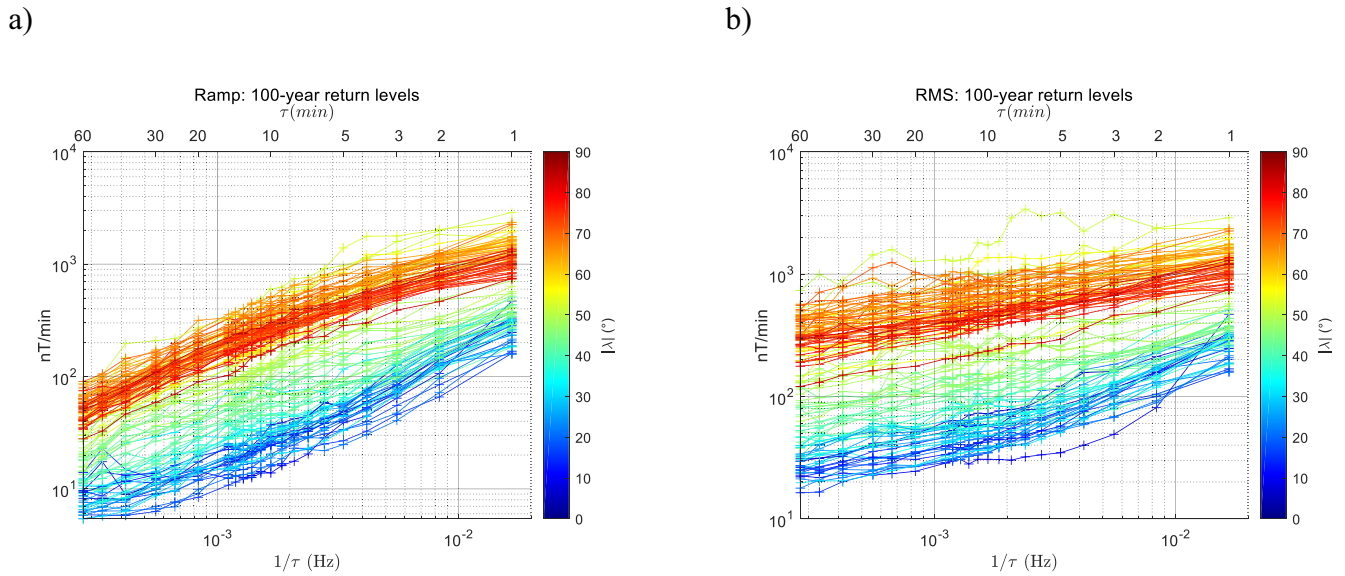


Figure 11. Hundred-year return levels for (a) R_n , and (b) S_n , for $n = 1\text{--}60$ min (top axis), plotted against the sampling frequency (bottom axis). Maximum likelihood estimate values are shown for all 125 magnetometer sites, colored according to absolute geomagnetic latitude, $|\lambda|$.

in the east direction, where σ is the conductivity of the ground. Equation 9 is known as the “basic equation of magnetotellurics” and is valid under the assumptions that the permittivity $\epsilon \ll \sigma/2\pi f$ and the conductivity of the air above the surface is negligible. As discussed by Wait (1962), the plane wave approximation (Equation 8) may be used provided there is negligible change in the incident wavefield amplitude over a lateral scale equal to the “skin depth” of the ground. Considering an additional orthogonal component of the magnetic field B_E , we may write Equation 9 more generally as

$$\begin{pmatrix} E_N \\ E_E \end{pmatrix} = \begin{pmatrix} 0 & Z \\ -Z & 0 \end{pmatrix} \begin{pmatrix} B_N \\ B_E \end{pmatrix} / \mu_0 \quad (10)$$

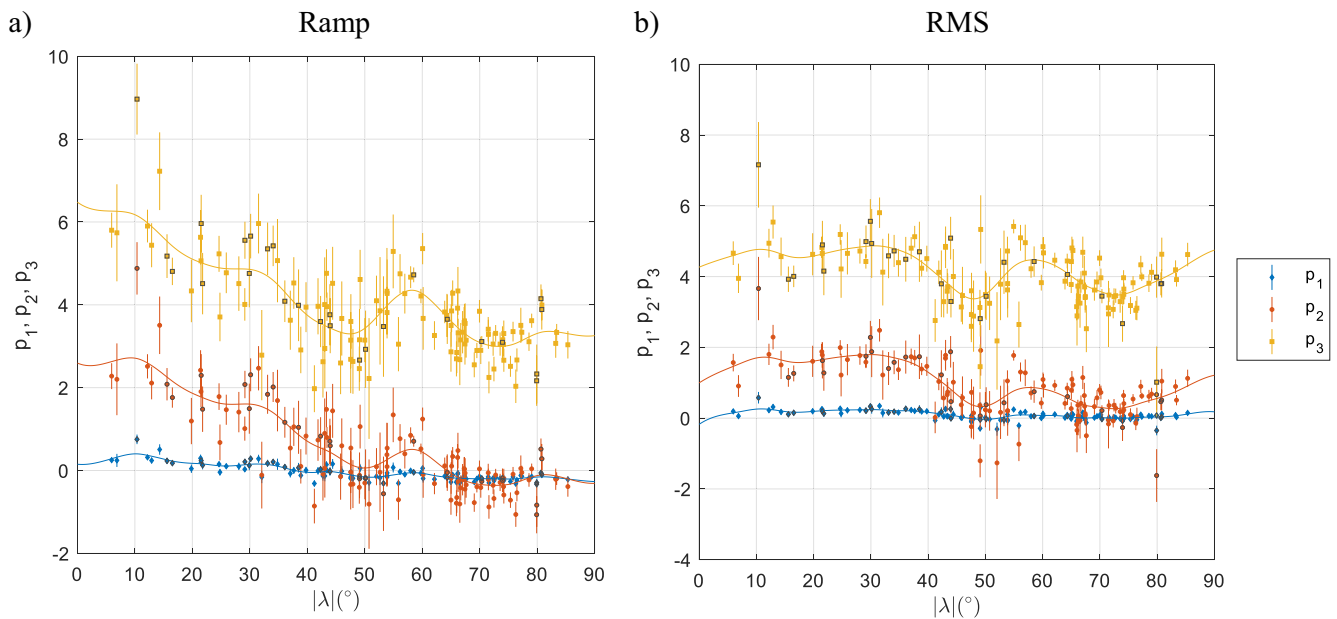


Figure 12. Coefficients of the polynomial (6) best fitted to 100-year return levels of $|dB_n / dt|$, presented in the same format as Figure 5. (a) R_n , and (b) S_n . Markers for Southern Hemisphere sites have a gray outline. RMS, root-mean-square.

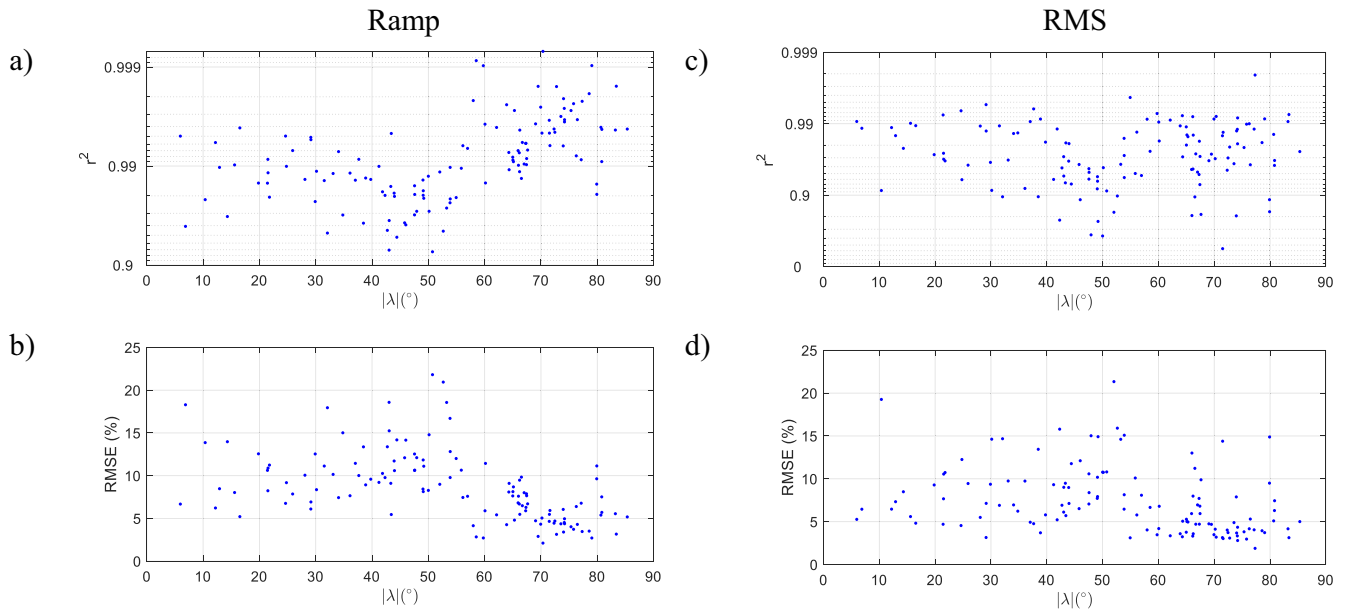


Figure 13. Goodness of fit metrics for the polynomial (6) fit to $\log_{RL100}(\log f_s)$ for (a and b) Ramp, and (c and d) root-mean-square (RMS) fluctuations. Top panels (a and c) are coefficients of determination, r^2 . Bottom panels (b and d) are the RMS of residuals.

where

$$Z = \sqrt{\frac{2\pi f \mu_0}{\sigma}} e^{i\frac{\pi}{4}} \quad (11)$$

Thus, for a uniform half-space model earth, ρ_a would be invariant with frequency, f , and the components of Z would have a constant 45° phase for all f . The measurements in Figure 15 show that the apparent resistivity of the ground differs greatly between sites as is expected from the very different geological settings that give rise to the electrical response.

For each site, the off-diagonal components $\rho_{a(xy)}$ and $\rho_{a(yx)}$ are not of equal magnitude, which indicates that the MT transfer function introduces “directional anisotropy” (i.e., from Equation 10, $|E_N| \neq |E_E|$ when $|B_N| = |B_E|$). The diagonal terms $\rho_{a(xx)}$ and $\rho_{a(yy)}$ are nonzero (notably for Lerwick), suggesting some deviation from the simple half-space model (i.e., measurements imply a fully three-dimensional distribution of electrical resistivity).

Noting from Equation 8 that

$$\frac{dB_N}{dt} = i2\pi f B_N \quad (12)$$

and similarly for B_E , we may estimate the geoelectric field from the rate-of-change of the magnetic field:

$$\mathbf{E}(f) = \frac{1}{i2\pi f} \mathbf{Z}(f) \begin{pmatrix} \frac{dB_N}{dt}(f) \\ \frac{dB_E}{dt}(f) \end{pmatrix} \quad (13)$$

where \mathbf{Z} is determined from the empirical MT transfer function (\mathbf{Z}/μ) using the approximation $\mu \cong \mu_0$. In the ideal case of homogenous ground conductivity, Equations 13 and 11 indicate that the spectrum of $|E|$ is proportional to $f^{-0.5}$ times the spectrum of $|dB/dt|$ (i.e., it is low-pass filtered).

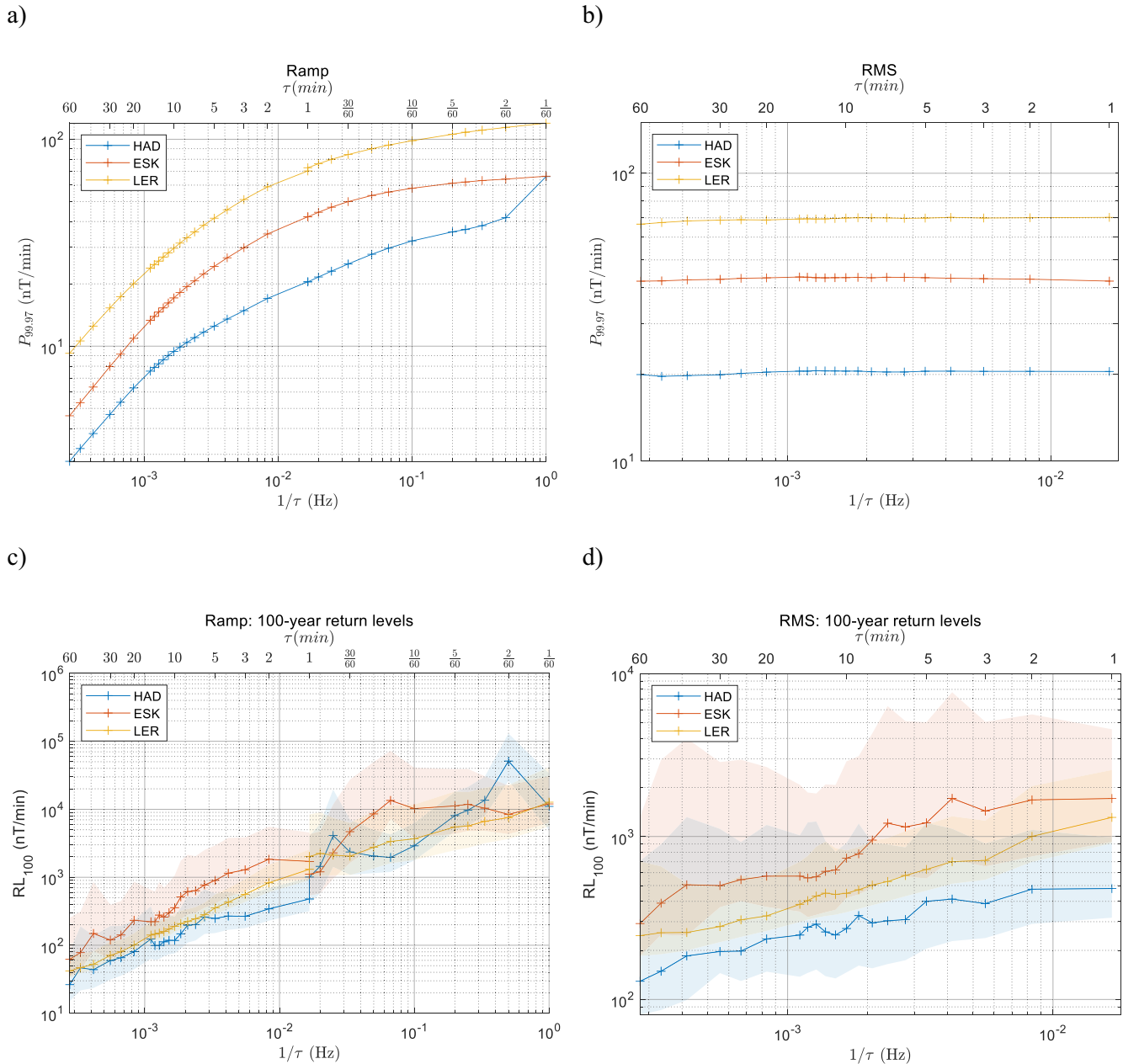


Figure 14. (a) $P_{99.97}$ of R_n , (b) $P_{99.97}$ of S_n , (c) 100-year return levels (RLs) of R_n , and (d) 100-year RL of S_n , for three UK sites. RLs are maximum likelihood estimates, while the shaded regions indicate 95% confidence intervals.

To estimate the amplitude of the geoelectric field expected to result from the 99.97th percentile of R_n for a range of frequencies, we modeled the waveform as a vertically propagated sinusoid $B_0 \sin(2\pi f)$ with amplitude $B_0 = \tau P_{99.97}/2$ and frequency $f = 1/(2\tau)$. This required a linear interpolation of the $P_{99.97}$ (Figure 14a) to frequencies recorded in the MT transfer function at each site (Figure 15). The resulting estimates of the magnitude $|E| = \sqrt{E_N^2 + E_E^2}$ from Equation 13 are presented in Figure 16a where circles represent B -field fluctuations confined to the N-S plane ($|B_N| = B_0; B_E = 0$) and asterisks represent B -field fluctuations in the E-W plane ($B_N = 0; |B_E| = B_0$). The two polarizations yield E -fields that differ in magnitude by a factor of up to 2 because the MT transfer function is not directionally isotropic and the ground impedance depends on all three coordinates (x , y , and z). At each UK site, exceedances of $P_{99.97}$ after declustering, occurred on average every 0.1–0.35 years over the range $\tau = 1$ –60 min, and so should be considered as large, but not extreme

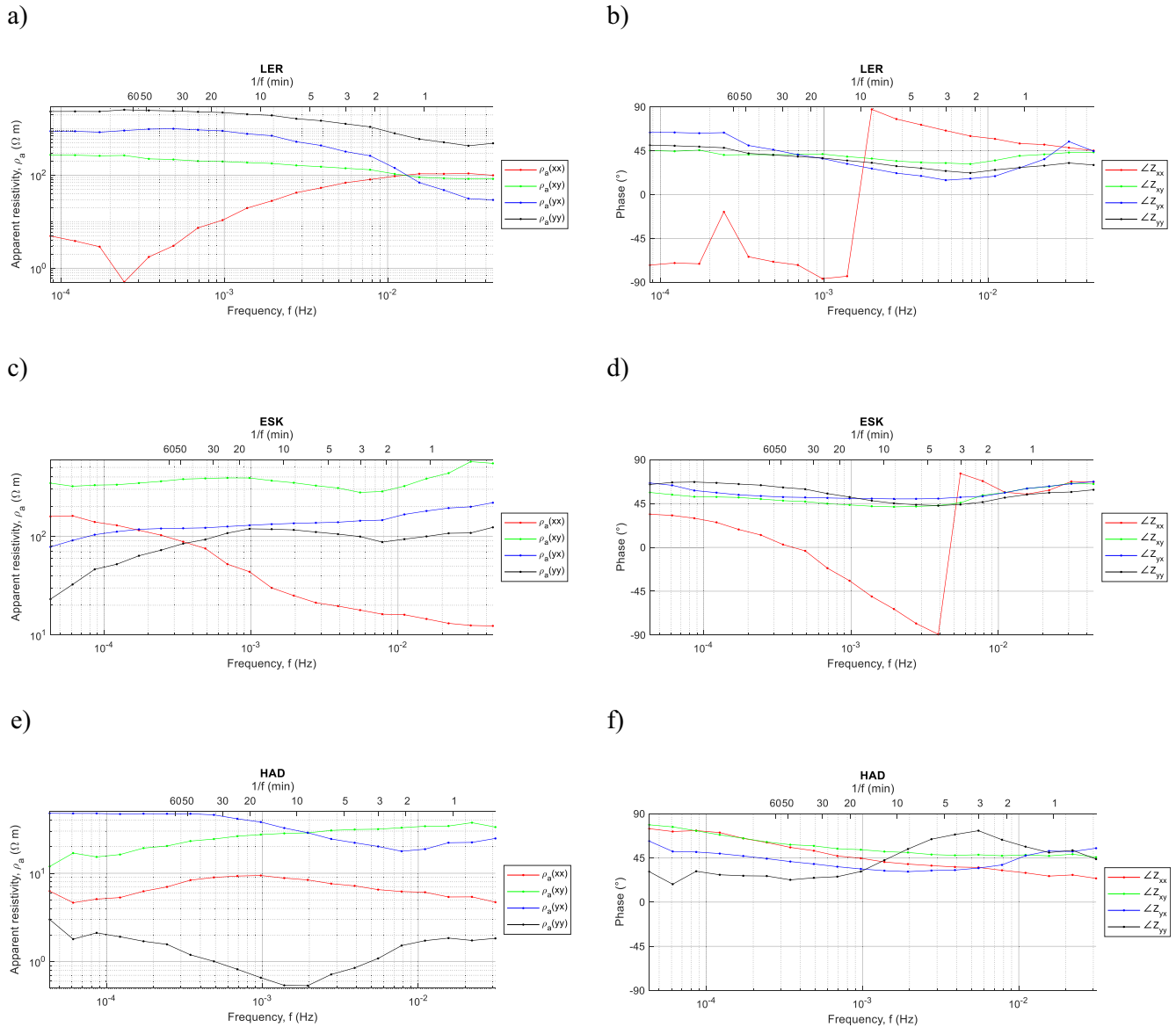


Figure 15. Apparent resistivity and phase of Z , determined empirically for (a and b) LER, (c and d) ESK, and (e and f) HAD magnetometers. Panels (a, c, and e) show the apparent resistivity, and panels (b, d, and f) show the phase.

values. Figure 16b presents the E -field magnitude for sinusoids with peak-to-peak amplitude ($2B_0$) equal to the 100-year RLs, R_n (from Figure 14c).

To put these values in context, an E field of 1–2 V/km over large distances can, depending on the grid topology, produce GIC that saturates the steel core of a HV transformer, which may lead to heating and potential failure of core components and the introduction of harmonics in the power system (Barnes et al., 1991). Winter et al. (2017) estimated the E field at UK latitudes associated with the 1859 storm—the largest geomagnetic storm on record (Carrington, 1859; Cliver & Dietrich, 2013)—to be ~ 9 V/km, and it is estimated that the 9-hr Hydro-Québec electricity blackout of March 1989 resulted from E fields of about 10 V/km (Barnes et al., 1991).

The predicted frequency dependences for the 99.97th percentile of $|E|$ (denoted $E_{99.97}$) take a very different form to those for the 100-year RLs (denoted E_{RL100}): E -field amplitudes at the 99.97th percentile (occurring several times a year) are greatest for sinusoid periods of ~ 20 min, while 1/100-year events have greatest

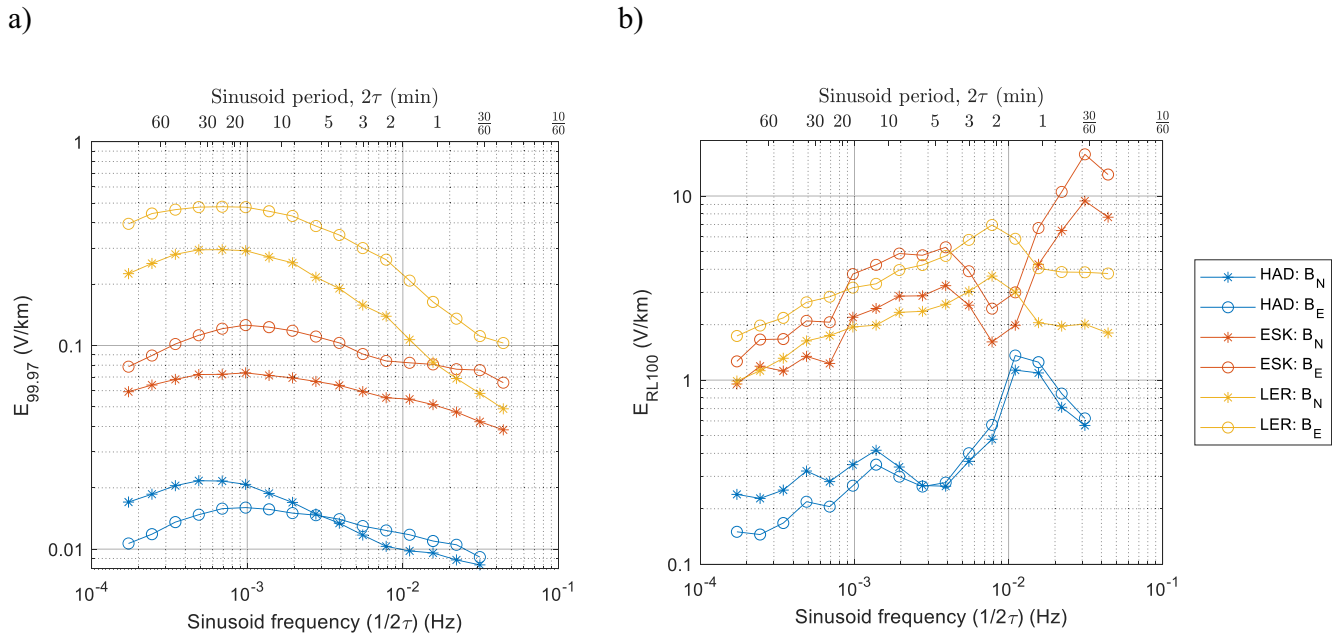


Figure 16. (a) 99.97th percentile and (b) 100-year RL of $|E|$ at three UK sites. Circles indicate fields modeled with sinusoidal B -field in the N-S plane, asterisks are for B in the E-W plane.

amplitude for periods between 30 s and 2 min. The observation that 100-year RL predictions vary greatly with sinusoid frequency has important implications when comparing and contrasting statistical studies evaluating extremes of $|E|$, which may have been based on different sinusoid frequencies.

Model estimates of the E field based on single-frequency components of the geomagnetic fluctuation have been reported by several authors (Bedrosian & Love, 2015; Beggan, 2015; Beggan et al., 2013; Love, Pulkkinen, et al., 2016). Love, Pulkkinen, et al. (2016) examined the amplitude of 4-min period sinusoids fitted to geomagnetic measurements (over sliding 10-min windows) and estimated extreme E -field amplitudes using empirical MT transfer functions at sites in the contiguous US ($\lambda \approx 40$ – 60°N). Only at the northern limit, in the northern mid-west states, did they find E_{RL100} exceeding 3 V/km, which is similar to the 3–5 V/km predicted in Figure 16 for LER ($\lambda = 58^\circ\text{N}$) for a 4-min sinusoid period. However, direct comparisons between sites cannot be made without considering differences in the surface impedance and its gradients. Bedrosian and Love (2015) illustrated this point by simulating the E fields generated by sinusoids with 10-, 100-, and 1,000-s periods using MT transfer functions from the EarthScope MT array in the Midwest US and showed that a constant-amplitude $B_0 = 500$ nT, 100-s period B field would induce $|E|$ of 2.7 V/km, averaged across all sites, but with values ranging from 0.15 to 16.8 V/km depending on the site. Similarly, Pulkkinen et al. (2012), by extrapolating a log-normal distribution of 10-s field data from 23 European sites (55° – 75°N geomagnetic), predicted E_{RL100} ranging from 5 V/km with a high-conductivity ground model to 20 V/km for poor-conductivity ground. Beggan et al. (2013) and Beggan (2015) also modeled the extreme E -field in the United Kingdom based on a conductivity model and B -fields modeled as sinusoids with periods, T , of 2, 10, and 30 min and amplitudes based on the 30-, 100-, and 200-year RLs of 1-min dB_h/dt predicted by Thomson et al. (2011). The 2-min E_{RL100} prediction of Beggan et al. (2013) shown in their Figure 6 (middle column) shows not only the high level of localization of the E field intensity, ranging from around 2 to 7 V/km, but also the importance of the direction of the inducing B -field (whether N-S or E-W aligned) for some locations. We intend to report further on the importance of directionality in extreme dB_h/dt statistics in a forthcoming publication.

There are, of course, limitations to “narrowband” models of geomagnetic events since, in practice, fluctuations will be broadband in nature and the frequency spectrum of any individual geomagnetic event will be unique. We have noted that many of the extreme events (exceeding $P_{99.97}$) identified in our data set occur simultaneously (within hours of each other) over a wide range of timescales (or frequencies), but our results

should not be used to infer a frequency spectrum of B or E fields for any given extreme geomagnetic event. For this information, the reader may refer to several studies of extreme values that have taken the approach of analyzing the E field produced during rare and intense geomagnetic storm periods and in some cases scaling up their effect to simulate 100-year RLS (e.g., Lotz & Danskin, 2017; Ngwira et al., 2013; Pulkkinen et al., 2012).

5. Conclusion

The importance of ULF waves in driving extreme geoelectric fields and GICs has received a great deal of interest in recent years (Belakhovsky et al., 2019; Hartinger et al., 2020; Heyns et al., 2020; Pulkkinen & Kataoka, 2006) and there is a need for a better understanding of the frequency dependence of the B and E field fluctuations driving GICs (e.g., Pulkkinen et al., 2017). Most previous statistical climatological studies of extreme values for E and dB_h/dt have been based on sampling at just one or two frequencies. In this paper, however, we have presented statistics of large ($P_{99.97}$) and extreme (e.g., 1/100-year) values for $|dB_h/dt|$ on a wide range of timescales, τ , from 1 to 60 min. At latitudes above the dayside cusp ($\lambda > 80^\circ$), for example, we find that occurrences of $|dB_h/dt|$ ramp changes above $P_{99.97}$ become tightly clustered in the few hours about local noon and the effect is greatest for longer timescales ($\tau \geq 30$ min). We have contrasted the statistics of ramp changes with those of the RMS of 1-min fluctuations over the same range of timescales and find, in particular, that in the auroral zone, for $\tau > 10$ min, the MLT of greatest occurrence of large RMS variation is from dawn to noon, indicative of strong ULF wave activity in this local time sector. The frequency ($1/\tau$) dependences (for both ramp changes and RMS variations) are found to be not a simple power law, but are well modeled by quadratic functions whose three coefficients vary predictably with geomagnetic latitude.

For three UK locations, we extended the data set to 1 Hz sampling frequency, and using a plane wave approximation and measured MT transfer functions, we derived the frequency dependence of the 99.97th percentile and 100-year RLS of the geoelectric field, E at those sites. For events occurring several times a year (at the 99.97th percentile), the induced E fields were greatest for fluctuations of a 20-min period, while the 1-in-100-year RLS were greatest for 0.5–2-min period fluctuations.

These statistics may be useful when inferring the likely extremes of $|dB_h/dt|$ or E over a wide frequency range based on studies that used a single sampling cadence. The distributions of extreme occurrence rates with latitude, local time, and season may also improve our understanding of the main ionospheric and magnetospheric drivers of GICs.

Appendix A

Here, it is demonstrated that the horizontal geoelectric field magnitude $|E|$ is proportional to R_n as defined in Equation 2 when using a half-space model for the impedance matrix. From Equation 10, the idealized half-space impedance is given by

$$\mathbf{Z} = \sqrt{\frac{2\pi f \mu_0}{\sigma}} e^{\frac{i\pi}{4}} \begin{pmatrix} 0 & 1 \\ -1 & 0 \end{pmatrix} \quad (\text{A1})$$

and for a sinusoidal horizontal magnetic field, $\mathbf{B} \equiv \begin{pmatrix} B_N \\ B_E \end{pmatrix}$, with frequency f (Hz), the horizontal geoelectric field is given by Equation 13

$$\mathbf{E} \equiv \begin{pmatrix} E_N \\ E_E \end{pmatrix} = \frac{1}{i2\pi f} \mathbf{Z} \begin{pmatrix} \frac{dB_N}{dt} \\ \frac{dB_E}{dt} \end{pmatrix} \quad (\text{A2})$$

Substituting Equation A1 into Equation A2 gives

$$\begin{pmatrix} E_N \\ E_E \end{pmatrix} = \frac{1}{i2\pi f} \sqrt{\frac{2\pi f \mu_0}{\sigma}} e^{i\pi/4} \begin{pmatrix} 0 & 1 \\ -1 & 0 \end{pmatrix} \begin{pmatrix} \frac{dB_N}{dt} \\ \frac{dB_E}{dt} \end{pmatrix} = \sqrt{\frac{\mu_0}{2\pi f \sigma}} e^{-i\pi/4} \begin{pmatrix} \frac{dB_E}{dt} \\ -\frac{dB_N}{dt} \end{pmatrix}$$

By comparing components it is observed that $|E_N| \propto |dB_E / dt|$ (where \propto denotes proportionality) and $|E_E| \propto |dB_N / dt|$, and so $|E| = \sqrt{E_N^2 + E_E^2} \propto R_n$, where R_n is defined using the expression in Equation 2. Approximate proportionality may be observed when the impedance Z differs only slightly from the half-space model of impedance in Equation A1.

Data Availability Statement

The 1-min cadence magnetometer data used in this paper are available from <https://supermag.jhuapl.edu> and described in Gjerloev (2012). One-second cadence UK magnetometer data are available from the British Geological Survey: http://www.geomag.bgs.ac.uk/data_service/data/home.html. The electric field data used to calculate the MT transfer functions are available within the ESA Space Weather framework: <https://swe.ssa.esa.int/BGS-federated>.

Acknowledgments

This work was funded by the UK Natural Environment Research Council (NERC) under grants NE/P016715/1 and NE/P017231/1 as part of the UK “Space Weather Impacts on Ground-based Systems” (SWIGS) project. Magnetometer data were provided by SuperMAG (available from <https://supermag.jhuapl.edu>) and the authors gratefully acknowledge contributions from the SuperMAG collaborators: Intermagnet; USGS, J. J. Love; CARISMA, PI I. Mann; CANMOS; The S-RAMP Database, PI K. Yumoto and Dr K. Shiokawa; The SPIDR database; AARI, PI Oleg Troshichev; The MACCS program, PI M. Engebretson, Geomagnetism Unit of the Geological Survey of Canada; GIMA; MEASURE, UCLA IGPP and Florida Institute of Technology; SAMBA, PI E. Zesta; 210 Chain, PI K. Yumoto; and SAMNET, PI F. Honary; The IMAGE magnetometer network, PI L. Juusola; AUTUMN, PI M. Connors; DTU Space, PI A. Willer; South Pole and McMurdo Magnetometer, PI’s L.J. Lanzarotti and A. T. Weatherax; ICE-STAR; RAPIDMAG; British Antarctic Survey; McMac, PI Dr P. Chi; BGS, PI Dr S. Macmillan; Pushkov Institute of Terrestrial Magnetism, Ionosphere and Radio Wave Propagation (IZMIRAN); GFZ, PI Dr J. Matzka; MFGI, PI B. Heilig; IGFAS, PI J. Reda; University of L’Aquila, PI M. Vellante; BCMT, V. Lesur and A. Chambodut; Data obtained in cooperation with Geoscience Australia, PI M. Costelloe; AALPIP, co-PIs B. Clauer and M. Hartinger; SuperMAG, PI J. W. Gjerloev; Sodankylä Geophysical Observatory, PI T. Raita; Polar Geophysical Institute, A. Yahnin and Y. Sakharov; Geological Survey of Sweden, G. Schwartz; Swedish Institute of Space Physics, M. Yamauchi; UiT the Arctic University of Norway, M. G. Johnsen; and Finnish Meteorological Institute, PI K. Kauristie.

References

- Adebesin, B. O., Pulkkinen, A., & Ngwira, C. M. (2016). The interplanetary and magnetospheric causes of extreme dB/dt at equatorial locations. *Geophysical Research Letters*, 43(22), 11501–11509. <https://doi.org/10.1002/2016GL071526>
- Akasofu, S.-I. (2017). Auroral substorms: Search for processes causing the expansion phase in terms of the electric current approach. *Space Science Reviews*, 212, 341–381. <https://doi.org/10.1007/s11214-017-0363-7>
- Angelopoulos, V., Baumjohann, W., Kennel, C. F., Coroniti, F. V., Kivelson, M. G., Pellat, R., et al. (1992). Bursty bulk flows in the inner central plasma sheet. *Journal of Geophysical Research*, 97, 4027–4039. <https://doi.org/10.1029/91JA02701>
- Apatenkov, S. V., Pilipenko, V. A., Gordeev, E. I., Viljanen, A., Juusola, L., Belakhovsky, V. B., et al. (2020). Auroral omega bands are a significant cause of large geomagnetically induced currents. *Geophysical Research Letters*, 47, e2019GL086677. <https://doi.org/10.1029/2019GL086677>
- Baker, G. J., Donovan, E. F., & Jackel, B. J. (2003). A comprehensive survey of auroral latitude Pc5 pulsation characteristics. *Journal of Geophysical Research*, 108(A10). <https://doi.org/10.1029/2002JA009801>
- Barnes, P. R., Rizy, D. T., McConnell, B. W., Tesche, F. M., & Taylor, E. R., Jr. (1991). *Electric utility industry experience with geomagnetic disturbances* (ORNL-6665, pp. 1–78). Oak Ridge National Lab. <https://doi.org/10.2172/1010842>
- Beamish, D., Clark, T. D. G., Clarke, E., & Thomson, A. W. P. (2002). Geomagnetically induced currents in the UK: Geomagnetic variations and surface electric fields. *Journal of Atmospheric and Solar-Terrestrial Physics*, 64(16), 1779–1792. [https://doi.org/10.1016/S1364-6826\(02\)00127-X](https://doi.org/10.1016/S1364-6826(02)00127-X)
- Bedrosian, P. A., & Love, J. J. (2015). Mapping geoelectric fields during magnetic storms: Synthetic analysis of empirical United States impedances. *Geophysical Research Letters*, 42, 10160–10170. <https://doi.org/10.1002/2015GL066636>
- Beggan, C. D. (2015). Sensitivity of geomagnetically induced currents to varying auroral electrojet and conductivity models. *Earth, Planets and Space*, 67(1). <https://doi.org/10.1186/s40623-014-0168-9>
- Beggan, C. D., Beamish, D., Richards, A., Kelly, G. S., & Alan, A. W. (2013). Prediction of extreme geomagnetically induced currents in the UK high-voltage network. *Space Weather*, 11(7), 407–419. <https://doi.org/10.1002/swe.20065>
- Beggan, C. D., Richardson, G. S., Baillie, O., Hübert, J., & Thomson, A. W. P. (2021). Geoelectric field measurement, modelling and validation during geomagnetic storms in the UK. *Journal of Space Weather and Space Climate*, 11, 37. <https://doi.org/10.1051/swsc/2021022>
- Belakhovsky, V., Pilipenko, V., Engebretson, M., Sakharov, Y., & Selivanov, V. (2019). Impulsive disturbances of the geomagnetic field as a cause of induced currents of electric power lines. *Journal of Space Weather and Space Climate*, 9, A18. <https://doi.org/10.1051/swsc/2019015>
- Boteler, D. H. (2000). Geomagnetic effects on the pipe-to-soil potentials of a continental pipeline. *Advances in Space Research*, 26(1), 15–20. [https://doi.org/10.1016/s0273-1177\(99\)01020-0](https://doi.org/10.1016/s0273-1177(99)01020-0)
- Boteler, D. H. (2021). Modeling geomagnetic interference on railway signaling track circuits. *Space Weather*, 19(1). <https://doi.org/10.1029/2020SW002609>
- Boteler, D. H., & Pirjola, R. J. (2017). Modeling geomagnetically induced currents. *Space Weather*, 15(1), 258–276. <https://doi.org/10.1002/2016SW001499>
- Buzulukova, N. (Ed.). (2017). *Extreme events in geospace: Origins, predictability, and consequences*. Elsevier.
- Cagniard, L. (1953). Basic theory of the magneto-telluric method of geophysical prospecting. *Geophysics*, 18, 605–635. <https://doi.org/10.1190/1.1437915>
- Cannon, P., Angling, M., Barclay, L., Curry, C., Dyer, C., Edwards, R., et al. (2013). *Extreme space weather: Impacts on engineered systems and infrastructure*. Royal Academy of Engineering. Retrieved from <http://www.raeng.org.uk/spaceweather>
- Carrington, R. C. (1859). Description of a singular appearance seen in the Sun on September 1, 1859. *Monthly Notices of the Royal Astronomical Society*, 20, 13–15. <https://doi.org/10.1093/mnras/20.1.13>
- Carter, B. A., Yizengaw, E., Pradipta, R., Halford, A. J., Norman, R., & Zhang, K. (2015). Interplanetary shocks and the resulting geomagnetically induced currents at the equator. *Geophysical Research Letters*, 42(16), 6554–6559. <https://doi.org/10.1002/2015GL065060>
- Chave, A. D., & Jones, A. G. (2012). *The magnetotelluric method*. Cambridge University Press. <https://doi.org/10.1017/CBO9781139020138>
- Cliver, E. W., & Dietrich, W. F. (2013). The 1859 space weather event revisited: Limits of extreme activity. *Journal of Space Weather and Space Climate*, 3, 1–15. <https://doi.org/10.1051/swsc/2013053>

- Coles, S. (2001). *An introduction to statistical modeling of extreme values*. Springer-Verlag Ltd.
- Crooker, N. U. (1992). Reverse convection. *Journal of Geophysical Research*, 97(A12), 19363. <https://doi.org/10.1029/92ja01532>
- Danskın, D. W., & Lotz, S. I. (2015). Analysis of geomagnetic hourly ranges. *Space Weather*, 13(8), 458–468. <https://doi.org/10.1002/2015SW001184>
- Dimmock, A. P., Rosenqvist, L., Hall, J.-O., Viljanen, A., Yordanova, E., Honkonen, I., et al. (2019). The GIC and geomagnetic response over Fennoscandia to the 7–8 September 2017 geomagnetic storm. *Space Weather*, 17, 989–1010. <https://doi.org/10.1029/2018SW002132>
- Engebretson, M. J., Glassmeier, K.-H., Stellmacher, M., Hughes, W. J., & Lühr, H. (1998). The dependence of high-latitude Pc5 wave power on solar wind velocity and on the phase of high-speed solar wind streams. *Journal of Geophysical Research*, 103(A11), 26271–26283. <https://doi.org/10.1029/97ja03143>
- Engebretson, M. J., Kirkevold, K. R., Steinmetz, E. S., Pilipenko, V. A., Moldwin, M. B., McCuen, B. A., et al. (2020). Interhemispheric comparisons of large nighttime magnetic perturbation events relevant to GICs. *Journal of Geophysical Research: Space Physics*, 125, e2020JA028128. <https://doi.org/10.1029/2020JA028128>
- Engebretson, M. J., Pilipenko, V. A., Ahmed, L. Y., Posch, J. L., Steinmetz, E. S., Moldwin, M. B., et al. (2019). Nighttime magnetic perturbation events observed in Arctic Canada: 1. Survey and statistical analysis. *Journal of Geophysical Research: Space Physics*, 124, 7442–7458. <https://doi.org/10.1029/2019JA026794>
- Engebretson, M. J., Pilipenko, V. A., Steinmetz, E. S., Moldwin, M. B., Connors, M. G., Boteler, D. H., et al. (2021). Nighttime magnetic perturbation events observed in Arctic Canada: 3. Occurrence and amplitude as functions of magnetic latitude, local time, and magnetic disturbance indices. *Space Weather*, 19, e2020SW002526. <https://doi.org/10.1029/2020SW002526>
- Engebretson, M. J., Steinmetz, E. S., Posch, J. L., Pilipenko, V. A., Moldwin, M. B., Connors, M. G., et al. (2019). Nighttime magnetic perturbation events observed in Arctic Canada: 2. Multiple-instrument observations. *Journal of Geophysical Research: Space Physics*, 124, 7459–7476. <https://doi.org/10.1029/2019JA026797>
- Engebretson, M. J., Yeoman, T. K., Oksavik, K., Søråas, F., Sigernes, F., Moen, J. I., et al. (2013). Multi-instrument observations from Svalbard of a traveling convection vortex, electromagnetic ion cyclotron wave burst, and proton precipitation associated with a bow shock instability. *Journal of Geophysical Research: Space Physics*, 118, 2975–2997. <https://doi.org/10.1002/jgra.50291>
- Erinmez, I. A., Kappenman, J. G., & Radasky, W. A. (2002). Management of the geomagnetically induced current risks on the national grid company's electric power transmission system. *Journal of Atmospheric and Solar-Terrestrial Physics*, 64(5–6), 743–756. [https://doi.org/10.1016/S1364-6826\(02\)00036-6](https://doi.org/10.1016/S1364-6826(02)00036-6)
- Eroshenko, E. A., Belov, A. V., Boteler, D., Gaidash, S. P., Lobkov, S. L., Pirjola, R., & Trichtchenko, L. (2010). Effects of strong geomagnetic storms on Northern railways in Russia. *Advances in Space Research*, 46(9), 1102–1110. <https://doi.org/10.1016/j.asr.2010.05.017>
- Falayi, E. O., Ogunmodimu, O., Bolaji, O. S., Ayanda, J. D., & Ojoniyi, O. S. (2017). Investigation of geomagnetic induced current at high latitude during the storm-time variation. *NRIAG Journal of Astronomy and Geophysics*, 6(1), 131–140. <https://doi.org/10.1016/j.nrjag.2017.04.010>
- Faraday, M. (1832). Experimental researches in electricity. *Philosophical Transactions of the Royal Society*, 122, 125–162. <https://doi.org/10.1098/rstl.1832.0006>
- Fiori, R. A. D., Boteler, D. H., & Gillies, D. M. (2014). Assessment of GIC risk due to geomagnetic sudden commencements and identification of the current systems responsible. *Space Weather*, 12, 76–91. <https://doi.org/10.1002/2013SW000967>
- Freeman, M. P., Forsyth, C., & Rae, I. J. (2019). The influence of substorms on extreme rates of change of the surface horizontal magnetic field in the United Kingdom. *Space Weather*, 17(6), 827–844. <https://doi.org/10.1029/2018SW002148>
- Friis-Christensen, E., McHenry, M. A., Clauer, C. R., & Vennerstrøm, S. (1988). Ionospheric traveling convection vortices observed near the polar cleft: A triggered response to sudden changes in the solar wind. *Geophysical Research Letters*, 15(3), 253–256. <https://doi.org/10.1029/GL015i003p00253>
- Gaunt, C. T. (2016). Why space weather is relevant to electrical power systems. *Space Weather*, 14(1), 2–9. <https://doi.org/10.1002/2015SW001306>
- Gilleland, E., & Katz, R. W. (2016). extRemes 2.0: An extreme value analysis package in R. *Journal of Statistical Software*, 72(8), 1–39. <https://doi.org/10.18637/jss.v072.i08>
- Girgis, R., & Vedante, K. (2012). *Effects of GIC on power transformers and power systems* (pp. 1–8). 44th International Conference on Large High Voltage Electric Systems (PES T&D). <https://doi.org/10.1109/TDC.2012.6281595>
- Gjerloev, J. W. (2011). A global ground-based magnetometer initiative. *Eos*, 90, 230–231. <https://doi.org/10.1029/2009EO270002>
- Gjerloev, J. W. (2012). The SuperMAG data processing technique. *Journal of Geophysical Research*, 117(9). <https://doi.org/10.1029/2012JA017683>
- Hao, Y. X., Zong, Q. G., Zhou, X. Z., Rankin, R., Chen, X. R., Liu, Y., et al. (2019). Global-scale ULF waves associated with SSC accelerate magnetospheric ultrarelativistic electrons. *Journal of Geophysical Research: Space Physics*, 124, 1525–1538. <https://doi.org/10.1029/2018JA026134>
- Haggood, M., Angling, M. J., Attrill, G., Bisi, M., Cannon, P. S., Dyer, C., et al. (2021). Development of space weather reasonable worst case scenarios for the UK National Risk Assessment. *Space Weather*, 19, e2020SW002593. <https://doi.org/10.1029/2020SW002593>
- Hartering, M. D., Shi, X., Lucas, G. M., Murphy, B. S., Kelbert, A., Baker, J. B. H., et al. (2020). simultaneous observations of geoelectric and geomagnetic fields produced by magnetospheric ULF waves. *Geophysical Research Letters*, 47, e2020GL089441. <https://doi.org/10.1029/2020GL089441>
- Heyns, M. J., Lotz, S. I., & Gaunt, C. T. (2020). Geomagnetic pulsations driving geomagnetically induced currents. *Space Weather*, 19, e2020SW002557. <https://doi.org/10.1029/2020sw002557>
- Hüser, R., & Wadsworth, J. L. (2020). Advances in statistical modeling of spatial extremes. *WIREs Computational Statistics*, e1537. <https://doi.org/10.1002/wics.1537>
- Ieda, A., Kauristie, K., Nishimura, Y., Miyashita, Y., Frey, H. U., Juusola, L., et al. (2018). Simultaneous observation of auroral substorm onset in Polar satellite global images and ground-based all-sky images. *Earth, Planets and Space*, 70(1). <https://doi.org/10.1186/s40623-018-0843-3>
- IEEE. (2015). *IEEE guide for establishing power transformer capability while under geomagnetic disturbances* (IEEE Std C57.163 2015). The Institute of Electrical and Electronics Engineers, Inc.
- Jankee, P., Chisepo, H., Adebayo, V., Oyedokun, D., & Gaunt, C. T. (2020). *Transformer models and meters in MATLAB and PSCAD for GIC and leakage dc studies*. 2020 International SAUPEC/RobMech/PRASA Conference, SAUPEC/RobMech/PRASA 2020. <https://doi.org/10.1109/SAUPEC/RobMech/PRASA48453.2020.9041060>
- Jorgensen, A. M., Spence, H. E., Hughes, T. J., & McDiarmid, D. (1999). A study of omega bands and Ps6 pulsations on the ground, at low altitude and at geostationary orbit. *Journal of Geophysical Research*, 104(A7), 14705–14715. <https://doi.org/10.1029/1998ja900100>

- Kappenman, J. G. (2003). Storm sudden commencement events and the associated geomagnetically induced current risks to ground-based systems at low-latitude and midlatitude locations. *Space Weather*, 1(3), 1016. <https://doi.org/10.1029/2003sw000009>
- Kappenman, J. G. (2004). The evolving vulnerability of electric power grids. *Space Weather*, 2, S01004. <https://doi.org/10.1029/2003SW000028>
- Kataoka, R., Fukunishi, H., & Lanzerotti, L. J. (2003). Statistical identification of solar wind origins of magnetic impulse events. *Journal of Geophysical Research*, 108(A12). <https://doi.org/10.1029/2003JA010202>
- Kelbert, A., Balch, C. C., Pulkkinen, A., Egbert, G. D., Love, J. J., Rigler, E. J., & Fujii, I. (2017). Methodology for time-domain estimation of storm time geoelectric fields using the 3-D magnetotelluric response tensors. *Space Weather*, 15(7), 874–894. <https://doi.org/10.1002/2017SW001594>
- Kelbert, A., Egbert, G. D., & Schultz, A. (2011). *IRIS DMC data services products: EMTF, the magnetotelluric transfer functions*. <https://doi.org/10.17611/DP/EMTF.1>
- Kelbert, A., Erofeeva, S., Trabant, C., Karstens, R., & Van Fossen, M. (2018). Taking magnetotelluric data out of the drawer. *Eos*, 99. <https://doi.org/10.1029/2018EO112859>
- Knipp, D. J. (2011). *Understanding space weather and the physics behind it*. McGraw-Hill Companies, Inc.
- Kozyreva, O. V., Pilipenko, V. A., Belakhovsky, V. B., & Sakharov, Y. A. (2018). Ground geomagnetic field and GIC response to March 17, 2015, storm. *Earth, Planets and Space*, 70, 157. <https://doi.org/10.1186/s40623-018-0933-2>
- Lanzerotti, L. J., Konik, R. M., Wolfe, A., Venkatesan, D., & MacLennan, C. G. (1991). Cusp latitude magnetic impulse events: 1. Occurrence statistics. *Journal of Geophysical Research*, 96(A8), 14009–14022. <https://doi.org/10.1029/91ja00567>
- Laundal, K. M., & Richmond, A. D. (2017). Magnetic coordinate systems. *Space Science Reviews*, 206, 27–59. <https://doi.org/10.1007/s11214-016-0275-y>
- Liou, K., Newell, P. T., Sibeck, D. G., Meng, C.-I., Brittnacher, M., & Parks, G. (2001). Observation of IMF and seasonal effects in the location of auroral substorm onset. *Journal of Geophysical Research*, 106(A4), 5799–5810. <https://doi.org/10.1029/2000JA003001>
- Liu, J., Angelopoulos, V., Zhou, X.-Z., & Runov, A. (2014). Magnetic flux transport by dipolarizing flux bundles. *Journal of Geophysical Research: Space Physics*, 119, 909–926. <https://doi.org/10.1002/2013JA019395>
- Lotz, S. I., & Danskin, D. W. (2017). Extreme value analysis of induced geoelectric field in South Africa. *Space Weather*, 15, 1347–1356. <https://doi.org/10.1002/2017SW001662>
- Love, J. J., & Chulliat, A. (2013). An international network of magnetic observatories. *Eos Transactions, American Geophysical Union*, 94(42), 373–374. <https://doi.org/10.1002/2013EO420001>
- Love, J. J., Coisson, P., & Pulkkinen, A. (2016). Global statistical maps of extreme-event magnetic observatory 1 min first differences in horizontal intensity. *Geophysical Research Letters*, 43(9), 4126–4135. <https://doi.org/10.1002/2016GL068664>
- Love, J. J., Pulkkinen, A., Bedrosian, P. A., Jonas, S., Kelbert, A., Rigler, E. J., et al. (2016). Geoelectric hazard maps for the continental United States. *Geophysical Research Letters*, 43(18), 9415–9424. <https://doi.org/10.1002/2016GL070469>
- McPherron, R. L. (2005). Magnetic pulsations: Their sources and relation to solar wind and geomagnetic activity. *Surveys in Geophysics*, 26(5), 545–592. <https://doi.org/10.1007/s10712-005-1758-7>
- Milan, S. E., Carter, J. A., Bower, G. E., Imber, S. M., Paxton, L. J., Anderson, B. J., et al. (2020). Dual-lobe reconnection and horse-collar auroras. *Journal of Geophysical Research: Space Physics*, 125(10). <https://doi.org/10.1029/2020JA028567>
- Milan, S. E., Clausen, L. B. N., Coxon, J. C., Carter, J. A., Walach, M.-T., Laundal, K., et al. (2017). Overview of solar wind–magnetosphere–ionosphere–atmosphere coupling and the generation of magnetospheric currents. *Space Science Reviews*, 206(1–4), 547–573. <https://doi.org/10.1007/s11214-017-0333-0>
- Molinski, T. S. (2002). Why utilities respect geomagnetically induced currents. *Journal of Atmospheric and Solar-Terrestrial Physics*, 64, 1765–1778. [https://doi.org/10.1016/S1364-6826\(02\)00126-8](https://doi.org/10.1016/S1364-6826(02)00126-8)
- NERC. (2017). *Transformer thermal impact assessment: Project 2013-03 (geomagnetic disturbance mitigation)* (pp. 1–16). North American Electricity Reliability Corporation. Retrieved from http://www.nerc.com/pa/Stand/Project201303GeomagneticDisturbanceMitigation/Thermal_Impact_Assessment_2017_October_Clean.pdf
- Nevanlinna, H., Tenhunen, P., Pirjola, R., Annanpalo, J., & Pulkkinen, A. (2001). Breakdown caused by a geomagnetically induced current in the Finnish telesystem in 1958. *Journal of Atmospheric and Solar-Terrestrial Physics*, 63(10), 1099–1103. [https://doi.org/10.1016/S1364-6826\(01\)00021-9](https://doi.org/10.1016/S1364-6826(01)00021-9)
- Newell, P. T., & Gjerloev, J. W. (2011). Evaluation of SuperMAG auroral electrojet indices as indicators of substorms and auroral power. *Journal of Geophysical Research*, 116, A12211. <https://doi.org/10.1029/2011JA016779>
- Ngwira, C. M., Pulkkinen, A., Kuznetsova, M. M., & Glocer, A. (2014). Modeling extreme “Carrington-type” space weather events using three-dimensional global MHD simulations. *Journal of Geophysical Research: Space Physics*, 119, 4456–4474. <https://doi.org/10.1002/2013JA019661>
- Ngwira, C. M., Pulkkinen, A., Wilder, F. D., & Crowley, G. (2013). Extended study of extreme geoelectric field event scenarios for geomagnetically induced current applications. *Space Weather*, 11, 121–131. <https://doi.org/10.1002/swe.20021>
- Ngwira, C. M., Sibeck, D., Silveira, M. V. D., Georgiou, M., Weygand, J. M., Nishimura, Y., & Hampton, D. (2018). A study of intense local dB/dt variations during two geomagnetic storms. *Space Weather*, 16(6), 676–693. <https://doi.org/10.1029/2018SW001911>
- Nikitina, L., Trichtchenko, L., & Boteler, D. H. (2016). Assessment of extreme values in geomagnetic and geoelectric field variations for Canada. *Space Weather*, 14(7), 481–494. <https://doi.org/10.1002/2016SW001386>
- Oyedokun, D. T. O., & Cilliers, P. J. (2018). Geomagnetically induced currents: A threat to modern power systems. In A. F. Zobaa, S. H. E. Abdel Aleem, & A. Y. Abdelaziz (Eds.), *Classical and recent aspects of power system optimization* (pp. 421–462). Academic Press. <https://doi.org/10.1016/B978-0-12-812441-3.00016-1>
- Pahud, D. M., Rae, I. J., Mann, I. R., Murphy, K. R., & Amalraj, V. (2009). Ground-based Pc5 ULF wave power: Solar wind speed and MLT dependence. *Journal of Atmospheric and Solar-Terrestrial Physics*, 71, 1082–1092. <https://doi.org/10.1016/j.jastp.2008.12.004>
- Pilipenko, V., Kozyreva, O., Belakhovsky, V., Engebretson, M. J., & Samsonov, S. (2010). Generation of magnetic and particle Pc5 pulsations during the recovery phase of strong magnetic storms. *Proceedings of the Royal Society A: Mathematical, Physical & Engineering Sciences*, 466(2123), 3363–3390. <https://doi.org/10.1098/rspa.2010.0079>
- Pilipenko, V. A., Fedorov, E. N., Hartinger, M. D., & Engebretson, M. J. (2019). Electromagnetic fields of magnetospheric ULF disturbances in the ionosphere: Current/voltage dichotomy. *Journal of Geophysical Research: Space Physics*, 124, 109–121. <https://doi.org/10.1029/2018JA026030>
- Pirjola, R. (1982). Estimation of the electric field on the Earth's surface during a geomagnetic variation. *Geophysica*, 20(2), 89–103.
- Pirjola, R. (2010). Derivation of characteristics of the relation between geomagnetic and geoelectric variation fields from the surface impedance for a two-layer earth. *Earth, Planets and Space*, 62(3), 287–295. <https://doi.org/10.5047/eps.2009.09.002>

- Pothier, N. M., Weimer, D. R., & Moore, W. B. (2015). Quantitative maps of geomagnetic perturbation vectors during substorm onset and recovery. *Journal of Geophysical Research: Space Physics*, *120*, 1197–1214. <https://doi.org/10.1002/2014JA020602>
- Pulkkinen, A., Bernabeu, E., Eichner, J., Beggan, C., & Thomson, A. W. P. (2012). Generation of 100-year geomagnetically induced current scenarios. *Space Weather*, *10*, S04003. <https://doi.org/10.1029/2011SW000750>
- Pulkkinen, A., Bernabeu, E., Thomson, A., Viljanen, A., Pirjola, R., Boteler, D., et al. (2017). Geomagnetically induced currents: Science, engineering, and applications readiness. *Space Weather*, *15*, 828–856. <https://doi.org/10.1002/2016SW001501>
- Pulkkinen, A., & Kataoka, R. (2006). S-transform view of geomagnetically induced currents during geomagnetic superstorms. *Geophysical Research Letters*, *33*(12), 3–6. <https://doi.org/10.1029/2006GL025822>
- Pulkkinen, A., Kataoka, R., Watari, S., & Ichiki, M. (2010). Modeling geomagnetically induced currents in Hokkaido, Japan. *Advances in Space Research*, *46*(9), 1087–1093. <https://doi.org/10.1016/j.asr.2010.05.024>
- Pulkkinen, A., Viljanen, A., Pajunpää, K., & Pirjola, R. (2001). Recording and occurrence of geomagnetically induced currents in the Finnish natural gas pipeline network. *Journal of Applied Geophysics*, *48*(4), 219–231. [https://doi.org/10.1016/S0926-9851\(01\)00108-2](https://doi.org/10.1016/S0926-9851(01)00108-2)
- Pulkkinen, A., Viljanen, A., & Pirjola, R. (2006). Estimation of geomagnetically induced current levels from different input data. *Space Weather*, *4*(8), S08005. <https://doi.org/10.1029/2006SW000229>
- Rogers, N. C., Wild, J. A., Eastoe, E. F., Gjerloev, J. W., & Thomson, A. W. P. (2020). A global climatological model of extreme geomagnetic field fluctuations. *Journal of Space Weather and Space Climate*, *10*, 5. <https://doi.org/10.1051/swsc/2020008>
- Russell, C. T., & McPherron, R. L. (1973). Semiannual variation of geomagnetic activity. *Journal of Geophysical Research*, *78*(1), 92–108. <https://doi.org/10.1029/ja078i001p00092>
- Saito, T. (1978). Long-period irregular magnetic pulsation, Pi3. *Space Science Reviews*, *21*, 427–467. <https://doi.org/10.1007/BF00173068>
- Shepherd, S. G. (2014). Altitude-adjusted corrected geomagnetic coordinates: Definition and functional approximations. *Journal of Geophysical Research: Space Physics*, *119*(9), 7501–7521. <https://doi.org/10.1002/2014JA020264>
- Simpson, F., & Bahr, K. (2005). *Practical magnetotellurics*. Cambridge University Press. <https://doi.org/10.1017/CBO9780511614095>
- Smirnov, M. Y. (2003). Magnetotelluric data processing with a robust statistical procedure having a high breakdown point. *Geophysical Journal International*, *152*(1), 1–7. <https://doi.org/10.1046/j.1365-246X.2003.01733.x>
- Smith, A. W., Freeman, M. P., Rae, I. J., & Forsyth, C. (2019). The influence of sudden commencements on the rate of change of the surface horizontal magnetic field in the United Kingdom. *Space Weather*, *17*(11), 1605–1617. <https://doi.org/10.1029/2019SW002281>
- Thomson, A. W. P., Dawson, E. B., & Reay, S. J. (2011). Quantifying extreme behavior in geomagnetic activity. *Space Weather*, *9*, S10001. <https://doi.org/10.1029/2011SW000696>
- Thomson, A. W. P., & Flower, S. M. (2021). Modernizing a global magnetic partnership. *Eos*, *102*. <https://doi.org/10.1029/2021EO156569>
- Thomson, A. W. P., Gaunt, C. T., Cilliers, P., Wild, J. A., Opperman, B., Mckinnell, L.-A., et al. (2010). Present day challenges in understanding the geomagnetic hazard to national power grids. *Advances in Space Research*, *45*(9), 1182–1190. <https://doi.org/10.1016/j.asr.2009.11.023>
- Töth, G., Meng, X., Gombosi, T. I., & Rastätter, L. (2014). Predicting the time derivative of local magnetic perturbations. *Journal of Geophysical Research: Space Physics*, *119*(1), 310–321. <https://doi.org/10.1002/2013JA019456>
- Trichtchenko, L., & Boteler, D. H. (2004). Modeling geomagnetically induced currents using geomagnetic indices and data. *IEEE Transactions on Plasma Science*, *32*(4), 1459–1467. <https://doi.org/10.1109/TPS.2004.830993>
- Vennerstrom, S. (1999). Dayside magnetic ULF power at high latitudes: A possible long-term proxy for the solar wind velocity? *Journal of Geophysical Research*, *104*(A5), 10145–10157. <https://doi.org/10.1029/1999ja900015>
- Viljanen, A. (1997). The relation between geomagnetic variations and their time derivatives and implications for estimation of induction risks. *Geophysical Research Letters*, *24*(6), 631–634. <https://doi.org/10.1029/97GL00538>
- Viljanen, A., Nevanlinna, H., Pajunpää, K., & Pulkkinen, A. (2001). Time derivative of the horizontal geomagnetic field as an activity indicator. *Annales Geophysicae*, *19*(9), 1107–1118. <https://doi.org/10.5194/angeo-19-1107-2001>
- Viljanen, A., Wintoft, P., & Wik, M. (2015). Regional estimation of geomagnetically induced currents based on the local magnetic or electric field. *Journal of Space Weather and Space Climate*, *5*, A24. <https://doi.org/10.1051/swsc/2015022>
- Wait, J. R. (1962). Theory of magneto-telluric fields. *Journal of Research of the National Bureau of Standards—D. Radio Propagation*, *66D*(5), 509–541. <https://doi.org/10.6028/jres.066D.052>
- Wang, H., Lühr, H., Ma, S. Y., & Ritter, P. (2005). Statistical study of the substorm onset: Its dependence on solar wind parameters and solar illumination. *Annales Geophysicae*, *23*(6), 2069–2079. <https://doi.org/10.5194/angeo-23-2069-2005>
- Wang, H., Ridley, A. J., & Lühr, H. (2008). SWMF simulation of field-aligned currents for a varying northward and duskward IMF with nonzero dipole tilt. *Annales Geophysicae*, *26*(6), 1461–1477. <https://doi.org/10.5194/angeo-26-1461-2008>
- Watanabe, M., Kabin, K., Sofko, G. J., Rankin, R., Gombosi, T. I., Ridley, A. J., & Clauer, C. R. (2005). Internal reconnection for northward interplanetary magnetic field. *Journal of Geophysical Research*, *110*(A6). <https://doi.org/10.1029/2004JA010832>
- Watari, S., Kunitake, M., Kitamura, K., Hori, T., Kikuchi, T., Shiokawa, K., et al. (2009). Measurements of geomagnetically induced current in a power grid in Hokkaido, Japan. *Space Weather*, *7*(3). <https://doi.org/10.1029/2008SW000417>
- Wei, D., Dunlop, M. W., Yang, J., Dong, X., Yu, Y., & Wang, T. (2021). Intense dB/dt variations driven by near-Earth Bursty Bulk Flows (BBFs): A case study. *Geophysical Research Letters*, *48*. <https://doi.org/10.1029/2020GL091781>
- Weigel, R. S., Vassiliadis, D., & Klimas, A. J. (2002). Coupling of the solar wind to temporal fluctuations in ground magnetic fields. *Geophysical Research Letters*, *29*(19), 1915. <https://doi.org/10.1029/2002GL014740>
- Wik, M., Pirjola, R., Lundstedt, H., Viljanen, A., Wintoft, P., & Pulkkinen, A. (2009). Space weather events in July 1982 and October 2003 and the effects of geomagnetically induced currents on Swedish technical systems. *Annales Geophysicae*, *27*(4), 1775–1787. <https://doi.org/10.5194/angeo-27-1775-2009>
- Wild, J. A., Woodfield, E. E., Donovan, E., Fear, R. C., Grocott, A., Lester, M., et al. (2011). Midnight sector observations of auroral omega bands. *Journal of Geophysical Research*, *116*(A5), A00130. <https://doi.org/10.1029/2010JA015874>
- Wild, J. A., Yeoman, T. K., Eglitis, P., & Opgenoorth, H. J. (2000). Multi-instrument observations of the electric and magnetic field structure of omega bands. *Annales Geophysicae*, *18*(1), 99–110. <https://doi.org/10.1007/s00585-000-0099-6>
- Winter, L. M., Gannon, J., Pernak, R., Huston, S., Quinn, R., Pope, E., et al. (2017). Spectral scaling technique to determine extreme Carrington-level geomagnetically induced currents effects. *Space Weather*, *15*, 713–725. <https://doi.org/10.1002/2016SW001586>
- Wintoft, P. (2005). Study of the solar wind coupling to the time difference horizontal geomagnetic field. *Annales Geophysicae*, *23*(5), 1949–1957. <https://doi.org/10.5194/angeo-23-1949-2005>
- Wintoft, P., Viljanen, A., & Wik, M. (2016). Extreme value analysis of the time derivative of the horizontal magnetic field and computed electric field. *Annales Geophysicae*, *34*, 485–491. <https://doi.org/10.5194/angeo-34-485-2016>

- Wintoft, P., Wik, M., Lundstedt, H., & Eliasson, L. (2005). Predictions of local ground geomagnetic field fluctuations during the 7-10 November 2004 events studied with solar wind driven models. *Annales Geophysicae*, 23(9), 3095–3101. <https://doi.org/10.5194/angeo-23-3095-2005>
- Wintoft, P., Wik, M., & Viljanen, A. (2015). Solar wind driven empirical forecast models of the time derivative of the ground magnetic field. *Journal of Space Weather and Space Climate*, 5(A7). <https://doi.org/10.1051/swsc/2015008>
- Zesta, E., Hughes, W. J., & Engebretson, M. J. (2002). A statistical study of traveling convection vortices using the Magnetometer Array for Cusp and Cleft Studies. *Journal of Geophysical Research*, 107(A10). <https://doi.org/10.1029/1999JA000386>
- Zhang, X. Y., Zong, Q.-G., Wang, Y. F., Zhang, H., Xie, L., Fu, S. Y., et al. (2010). ULF waves excited by negative/positive solar wind dynamic pressure impulses at geosynchronous orbit. *Journal of Geophysical Research*, 115, A10221. <https://doi.org/10.1029/2009JA015016>
- Zhao, H., & Zong, Q.-G. (2012). Seasonal and diurnal variation of geomagnetic activity: Russell-McPherron effect during different IMF polarity and/or extreme solar wind conditions. *Journal of Geophysical Research*, 117, A11222. <https://doi.org/10.1029/2012JA017845>
- Ziesolleck, C. W. S., & McDiarmid, D. R. (1995). Statistical survey of auroral latitude Pc5 spectral and polarization characteristics. *Journal of Geophysical Research*, 100(A10), 19299. <https://doi.org/10.1029/95ja00434>